Bioactive Materials 42 (2024) 1–17

Contents lists available at ScienceDirect

Bioactive Materials

journal homepage: www.keaipublishing.com/en/journals/bioactive-materials

Cobalt ions-derived nanoenzyme array for endosseous neural network reconstruction and osseointegration

Xinmei Cai [a,1], Meng Yu [a,**,1], Bo Li [a], Yingang Zhang [b], Yong Han [a,b,*]

[a] State Key Laboratory for Mechanical Behavior of Materials, Xi'an Jiaotong University, Xi'an, 710049, China
[b] Department of Orthopaedics, The First Affiliated Hospital College of Medicine, Xi'an Jiaotong University, Xi'an, 710061, China

ARTICLE INFO

Keywords:
Cobalt ions-derived nanoenzyme
Neurogenic factors
Mesenchymal stem cells
Neural differentiation
Neurovascularized osseointegration

ABSTRACT

Interactions between bone cells and neurocytes are crucial for endosseous nerve and ensuing bone regeneration. However, absence of neural stem cells in bone makes the innervation of implant osseointegration a major challenge. Herein, a nanorod-like array of sodium hydrogen titanate (ST) co-doped with Co^{2+} and Co^{3+}, namely STC_h that behaves as a reactive oxygen species (ROS)-scavenging enzyme, was hydrothermally formed on Ti substrate. We show that the doped Co^{2+} and Co^{3+} locate at TiO_6 octahedral interlayers and within octahedra of STC_h lattice, appearing releasable and un-releasable, respectively, leading to an increase in Co^{3+}/Co^{2+} ratio and enzyme activity of the array with immersion. The nanoenzyme-released Co^{2+} triggers macrophages (MΦs) towards M1 phenotype, then the nanoenzyme scavenges extracellular ROS inducing M1-to-M2 transition. The neurogenic factors secreted by STC_h-regulated MΦs, in combination with the released Co^{2+}, promote mesenchymal stem cells to differentiate into neurons and Schwann cells compared to sole $Co^{2+}$and ST. STC_h array greatly enhances nerve reconstruction, type-H capillary formation and ensuing osseointegration in normal rat bone, and antibacteria via engulfing *S. aureus* by MΦs and osteogenesis in infective case. This nanoenzyme provides an alternative strategy to orchestrate endosseous nerve regeneration for osseointegration without loading exogenous neurotrophins in implants.

1. Introduction

Osseointegration of orthopaedic implants is formed via inducing *de novo* bone formation on their surfaces, which is initiated by immune cells-derived inflammatory responses, involving the interactions of cells such as macrophages (MΦs), mesenchymal stem cells (MSCs), endothelial cells (ECs) and the others in order [1]. Bone is recently found to be highly innervated by endosseous sensory nerve and sympathetic nerve [2], these nerves are essential upstream regulators of neovascularization and osteogenesis [3]. For example, neuropeptides such as sensory nerve-secreted calcitonin gene-related peptide (CGRP) and substance P (SP) could promote angiogenesis and osteogenesis by upregulating vascular endothelial growth factor A (VEGF-A) and bone morphogenetic protein 2 (BMP2) [2], while sympathetic nerve-secreted vasoactive intestinal peptide (VIP) could promote osteogenesis by upregulating Wnt/β-catenin signaling pathway and suppressing osteoclastogenesis [2]. Neurotrophins, such as nerve growth factor (NGF) and brain-derived neurotrophic factor (BDNF) secreted by sensory nerve, are also required for bone formation and vascularization [2,4,5]. While sensory fibers are parallel to blood vessels in bone, neuropeptide Y (NPY) and tyrosine hydroxylase (TH) positive sympathetic fibers were identified to wrap around blood vessels [5–7].

Endosseous nerve fibers comprise neuronal axons and surrounding Schwann cells [2,6], however, their regeneration and ensuing innervation of osseointegration hardly achieve by neurogenic differentiation of neural stem cells due to their absence in bone, bone marrow and periosteum [2]. As a kind of pluripotent stem cells abundant in bone, MSCs are shown to commit to osteoblasts, adipocytes and chondrocytes, but are unable to spontaneously differentiate into neural cells [8,9]. Recently, MSCs have been proven to transdifferentiate into neural cells by additional chemical stimulations, such as neuron-like cells by materials-loaded and released neurotrophins like NGF or BDNF [10,11]

Peer review under responsibility of KeAi Communications Co., Ltd.
* Corresponding author. State Key Laboratory for Mechanical Behavior of Materials, Xi'an Jiaotong University, Xi'an, 710049, China.
** Corresponding author.
E-mail addresses: ailsayu1988@mail.xjtu.edu.cn (M. Yu), yonghan@mail.xjtu.edu.cn (Y. Han).
[1] These authors contributed equally.

https://doi.org/10.1016/j.bioactmat.2024.08.005
Received 7 June 2024; Received in revised form 20 July 2024; Accepted 7 August 2024

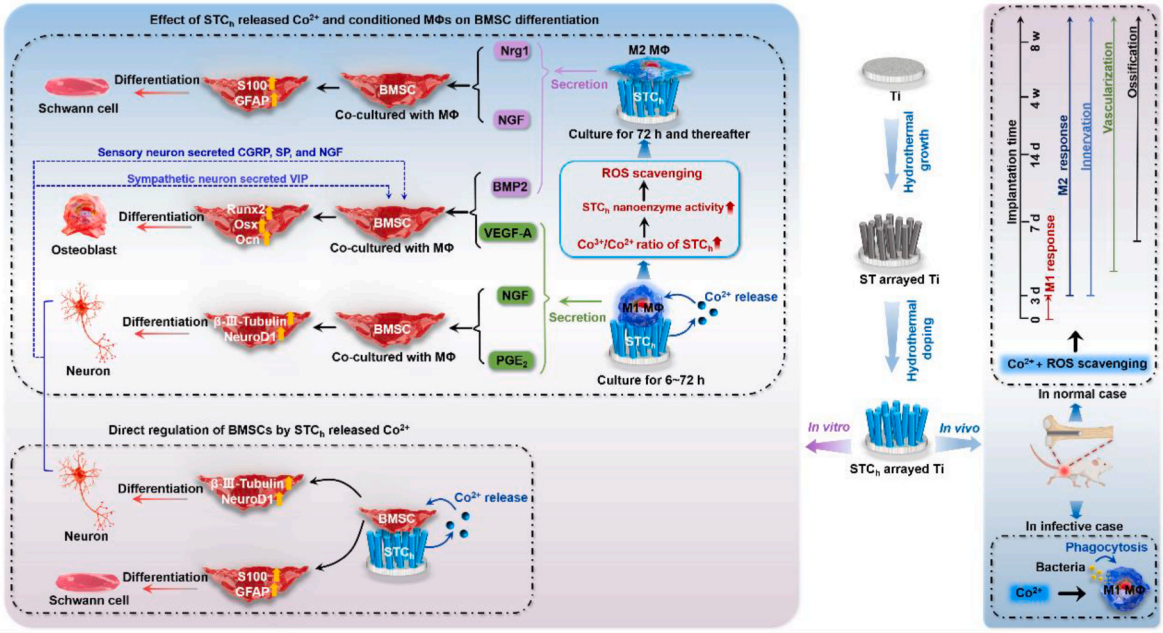

Scheme 1. Schematic illustration showing the fabrication procedures for a nanorod-like array of STC_h — sodium hydrogen titanate (ST) co-doped with Co^{2+} and Co^{3+} to achieve endosseous neural network reconstruction and osseointegration in normal case and antibacteria through phagocytosis of *S. aureus* by MΦs in infective case.

and ions of Ca^{2+} [12], Mg^{2+} [13], Fe^{3+} [14] or Si^{4+} [15], as well as Schwann cells by materials-loaded and released neurotrophins like NGF or neuregulin 1 (Nrg1) [16,17] and ions of Ca^{2+}, Mg^{2+} or Si^{4+} [18]. Although the neurotrophins show a greater impact on neural differentiation of MSCs than ions [19], the short half-lives of these biological factors extremely limit their effectiveness in clinic [20,21]. Thereby, the strategy to promote neural differentiation of MSCs with exogenous neurotrophins loading within materials for endosseous nerve regeneration is expected to be alternative.

Dependent on the local cues, MΦs may polarize towards a pro-inflammatory (M1) or a pro-healing (M2) phenotype to secret diverse cytokines influencing cell migration, angiogenesis and osteogenesis. For instance, M1 cells-secreted tumor necrosis factor-α (TNF-α), interleukin-1β (IL-1β) and VEGF-A as well as M2 cells-secreted platelet-derived growth factor-BB (PDGF-BB), transforming growth factor-β1 (TGF-β1) and stromal cell derived factor-1 (SDF-1) are known to promote MSC migration [1,22]. M1 cells-secreted VEGF-A as well as M2 cells-secreted PDGF-BB, angiopoietin-1 (ANG1) and SDF-1 are shown to promote the migration and sprouting of ECs [1,22]. M1 cells-secreted VEGF-A and M2 cells-secreted IL-4, IL-10, PDGF-BB, BMP2 and TGF-β1 are given to promote the recruitment and osteo-differentiation of MSCs [1,22,23]. Besides these angiogenic/osteogenic factors, MΦs have been recently demonstrated to secrete neurotrophic factors, such as NGF [24–26], glial cell line-derived neurotrophic factor (GDNF) [26], BDNF [27] and prostaglandin E_2 (PGE_2) [28] by M1 cells as well as BDNF [27], NGF [24,25] and TGF-β1 [29] by M2 cells, and all the factors contribute to the neuronal differentiation of MSCs [26,27,29–32]. Also, VEGF-A secreted by M1 cells and IL-10, NGF and Nrg1 secreted by M2 cells [33] were found to promote MSCs towards Schwann cells [34–36]. Therefore, it is an expected strategy to trigger the neural differentiation of MSCs by modulating the phenotype of MΦs to endogenously secrete the aforementioned cytokines.

Given that MΦs in sustained M1 phenotype could produce copious extracellular reactive oxygen species (ROS) such as H_2O_2 and $\bullet O^{2-}$, resulting in delayed angiogenesis and osteogenesis [37], it is vital to endow materials with ROS-scavenging property for M1-to-M2 shift. Inspired by the native ROS-scavenging enzymes such as superoxide dismutase (SOD) known to remove $\bullet O^{2-}$ and catalase (CAT) known to remove H_2O_2 [37], several SOD- and CAT-mimetics, especially Fe^{2+}-Fe^{3+} [37], Mn^{2+}-Mn^{4+} [38] or Ce^{3+}-Ce^{4+} [39] co-doped materials have been developed recently. Among them, the high atomic ratios of Fe^{3+}/Fe^{2+}, Mn^{4+}/Mn^{2+} and Ce^{4+}/Ce^{3+} in the crystal lattices of materials showed to decrease extracellular ROS levels and consequently resulted in M1-to-M2 phenotype switch [37–39]. Notably, cobalt ions also exist in multiple valence states, predominantly in divalence and trivalence [40]. Although the Co^{2+} ions stemming from $CoCl_2$ were shown to facilitate M1 polarization [41], whether the Co^{2+}-Co^{3+} co-doped materials have the effect of SOD-/CAT-mimetic enzyme to scavenge ROS or not and in which manner the Co^{2+} and Co^{3+} incorporate into the crystal lattices of materials remain to be explored.

In this work, we optimally fabricated a nanorod-like array of STC_h — sodium hydrogen titanate (ST) co-doped with Co^{2+} and Co^{3+} on Ti using hydrothermal growth and incorporation, and drew main results to present in Scheme 1. Particularly, STC_h array presents the doped Co^{2+} at TiO_6 octahedral interlayers and Co^{3+} in octahedra, not only spontaneously releasing Co^{2+} but also acting as a novel SOD/CAT-like nanoenzyme to scavenge ROS and this effect being enhanced with solution immersion. *In vitro*, STC_h derives bone marrow-derived MSCs (BMSCs) to differentiate into neurons and Schwann cells via releasing Co^{2+}, also elicits MΦs in a strong M1 response initially and thereafter in M2 response via Co^{2+} stimulus and ROS scavenging. Under synergistic actions of released Co^{2+} and conditioned MΦs-secreted neurogenic factors, STC_h array renders BMSCs to differentiate into more sensory neurons but less sympathetic neurons. In rat bone, STC_h strongly accelerates neural network (especially sensory fibers) reconstruction, angiogenesis (particularly type-H capillaries) and osseointegration in normal case, and a strong antibacterial effect through phagocytosis of *Staphylococcus aureus (S. aureus)* by MΦs in infective case. It provides a new insight into orchestrating endosseous neural network reconstruction for osseointegration without loading exogenous neurotrophins in implants.

2. Materials and methods

2.1. Preparation and cobalt ion doping of nanorods-arrayed coatings

Pure titanium (Ti) were processed into disks (Ø 14 × 2 mm) and

pillars (Ø 1 × 10 mm), followed by cleaning with acetone, ethanol and distilled water, as described in **Supplementary information (SI) 1.1**. A two-step hydrothermal treatment was performed to obtain ST nanorod arrays grown on the un-etched (UE) and acid-etched (AE) Ti. In brief, each Ti was placed in an autoclave containing 10 mL of 1 M NaOH (Sigma-Aldrich, USA) solution and hydrothermally treated at 100 °C for 90 min. Then, each of the obtained samples was further immersed in 10 mL of 0.5 M NaOH solution and hydrothermally treated at 220 °C for 210 min. The obtained ST array coated on the un-etched and acid-etched Ti samples were named UE-ST, AE0.5-ST, AE5-ST, and AE10-ST, respectively. Based on the results displayed in **Fig. S1**, the following ST specifically refers to AE5-ST. For doping of cobalt ions, the ST-arrayed Ti discs were placed in autoclaves containing $[Co^{2+}]_{as}$ of 0.05, 0.1, 10, and 50 mM, respectively, and hydrothermally doped at 100 °C for 2 h. The array was hydrothermally doped at $[Co^{2+}]_{as}$ of 10 mM, namely STC_h. The STC_h-arrayed Ti discs were further immersed in a phosphate-balanced solution (PBS, Servicebio, China) at 37 °C for 14 days without refreshing. The obtained array was named STC_h-I.

2.2. Ionic release and ROS scavenging capacity of the arrays

The STC_h-arrayed Ti discs were immersed in *Dulbecco's modified Eagle's medium* (DMEM, Gibco, USA) at 37 °C for a series of periods (1, 3, 7, and 14 days) without refreshing the media. The discs-immersed media were collected to examine ionic concentrations of Na, Co, and Ti using an inductively coupled plasma-mass spectrometry (ICP-MS, Agilent 7700, USA).

The $\bullet O_2^-$, H_2O_2 and total ROS scavenging abilities of the arrays (ST, STC_h, and STC_h-I) as well as insoluble Co_2O_3-coated Ti were investigated comprehensively, involving a SOD detection kit (Nanjing Jiancheng Bioengineering Institute, China), a CAT detection kit (Nanjing Jiancheng Bioengineering Institute) and 1,1-diphenyl-2-picrylhydrazyl (DPPH) ethanol solution (0.5 mM, Sigma), respectively. The plain test solutions (namely BLANKs) and the test solutions supplemented with Co^{2+} in a dose equal to that released from STC_h for 14 days (namely SUPPL-Co^{2+}) were employed as controls. The adsorption of each resultant solution was tested by a Multiscan GO microreader (Thermo Fisher, USA). Five replicates were performed in each kind of ROS scavenging test.

2.3. In vitro cell response to ST and STC_h arrayed discs

2.3.1. Cell culture

BMSCs, MΦs (RAW264.7), and HUVECs were gifted by the Stem Cell Bank (Chinese Academy of Sciences, China), and their culture was described in detail in **SI 1.3.1**.

2.3.2. Responses of BMSCs on ST and STC_h arrayed discs

BMSCs seeded on tissue culture plate (TCP) and incubated in the culture medium supplemented with Co^{2+} in a concentration identical to that released from STC_h at the corresponding incubation time (namely TCP + Co^{2+}) were selected as controls. BMSCs seeded on TCP were incubated in the culture medium supplemented with 20 ng/mL NGF (Sigma-Aldrich) and 10 ng/mL basic fibroblast growth factor (bFGF, R&D Systems, USA) (namely TCP + NGF + bFGF) as a positive control for neuron, as well as BMSCs seeded on TCP being incubated in the culture medium supplemented with 5 μM forskolin (Beyotime, China) and 20 ng/mL bFGF (namely TCP + Forskolin + bFGF) as a positive control for Schwann cell. The mRNA expressions of hypoxia-inducible factor-1α (HIF-1α), β-III-Tubulin, neurogenic differentiation 1 (NeuroD1), glial fibrillary acidic protein (GFAP), S100, CGRP, SP, TH and LIM homeobox transcription factor 1 beta (Lmx1b) by adhered BMSCs were tested with real-time quantitative polymerase chain reaction (qRT-PCR) using a LightCycler@96 PCR analyzer (Roche, USA) and normalized to the housekeeping gene glyceraldehyde-3-phosphate dehydrogenase (Gapdh). The sequences of the above gene primers are listed in Table S1.

The protein expressions of β-III-Tubulin and GFAP by the committed BMSCs were detected using immunofluorescence staining, as described in detail in **SI**. The protein levels of HIF-1α, signal transducer and activator of transcription 3 (STAT3) and phosphorylated STAT3 (pSTAT3) in BMSCs of TCP + Co^{2+}, ST and STC_h groups for 24~168 h were examined by Western blot, as described in detail in **SI 1.3.3**.

2.3.3. Responses of MΦs on ST and STC_h arrayed discs

The phenotype-dependent mRNA expressions of M1 markers (CD86 and inducible nitric oxide synthase, iNOS) along with transcription factor HIF-1α and M2 markers (CD206 and Arginase 1, Arg1) in MΦs cultured on the discs for 6~168 h were tested with qRT-PCR. The sequences of the above gene primers are listed in Table S2.

The intracellular ROS of MΦs cultured on the discs were stained using 2′, 7′-dichloroflorofluorescin diacetate (DCFH-DA). The stained cells were then imaged using the Eclipse fluorescence microscope (Nikon, Japan).

The mRNA expressions of PTGES (synthase gene of PGE_2), NGF and Nrg1 by MΦs were tested with qRT-PCR. The sequences of the above gene primers are listed in Table S3. MΦs-secreted PGE_2, NGF and Nrg1 were respectively detected by corresponding ELISA kits (Elabscience, China).

2.3.4. Co-culture of BMSCs with MΦs on the ST and STC_h arrayed discs

The co-culture model was established as schemed in Fig. S10. BMSCs migrated to the bottom side of transwell membranes (Corning/Costar, USA) were used for the following examinations. After co-culture for 24~168 h, the mRNA and protein expressions of the neural-related markers were detected as mentioned in Section 2.3.2. The mRNA expressions of runt-related transcription factor 2 (Runx2), Osterix and Osteocalcin by the committed BMSCs were tested with qRT-PCR as mentioned before, and the sequences of the involved gene primers are listed in Table S4.

2.4. In vivo implantation tests of ST and STC_h pillars

2.4.1. Implantation of the arrayed pillars both in normal and infective cases

Male Sprague-Dawley (S-D) rats (~200 g weight) were employed for implantation of the pillars, which obeyed the guidelines and were approved by the Institutional Animal Care and Use Committee (IACUC) of Xi'an Jiaotong University (approval NO. XJTUAE2024-1921). Following anesthesia of the rats by isoflurane inhalations, a hole with a size of Φ1.5 mm × 10 mm was drilled on each of both hind limb femoral shafts of a rat, the ST- and STC_h-arrayed pillars were inserted into the holes followed by suturing of the muscle, subcutaneous tissue, and skin. After the surgery, the rats were housed in separate cages and allowed to move freely. In parallel, 100 μL of *S. aureus* (10^6 CFU/mL, ATCC 25293) was injected into the femoral medullary cavity of both hind limbs using a microsyringe to create the bacteria-infective model. The pillars were divided into four groups: ST, ST + LPS, ST + IL-4, and STC_h. For the group of ST + LPS or ST + IL-4, before the injection of ST-coated pillars, 100 μL of PBS containing 200 μg lipopolysaccharide (LPS, Sigma, USA) or 100 ng IL-4 (Sigma, USA) was injected into the femoral medullary cavities. No antibiotic was administered.

2.4.2. Immunofluorescent staining

Immunofluorescent staining was performed to test cellular responses and nerve fibers and blood vessels forming within the tissues adjacent to the pillars-removed spaces (PRS). In brief, the rats were sacrificed at a series of implantation periods: 1, 3, and 7 days, and the uninfected and *S. aureus*-infected femurs with implanted pillars were picked up, followed by fixation in 4 % PFA and decalcification in 10 % EDTA solution for 4 weeks. Then, the arrayed pillars were removed, and the resultant femurs were dehydrated in ethanol, embedded into paraffin, and cut into ~5 μm thin foils. The fluorescence staining examinations included MΦ phenotype indicative markers C–C chemokine receptor type 7

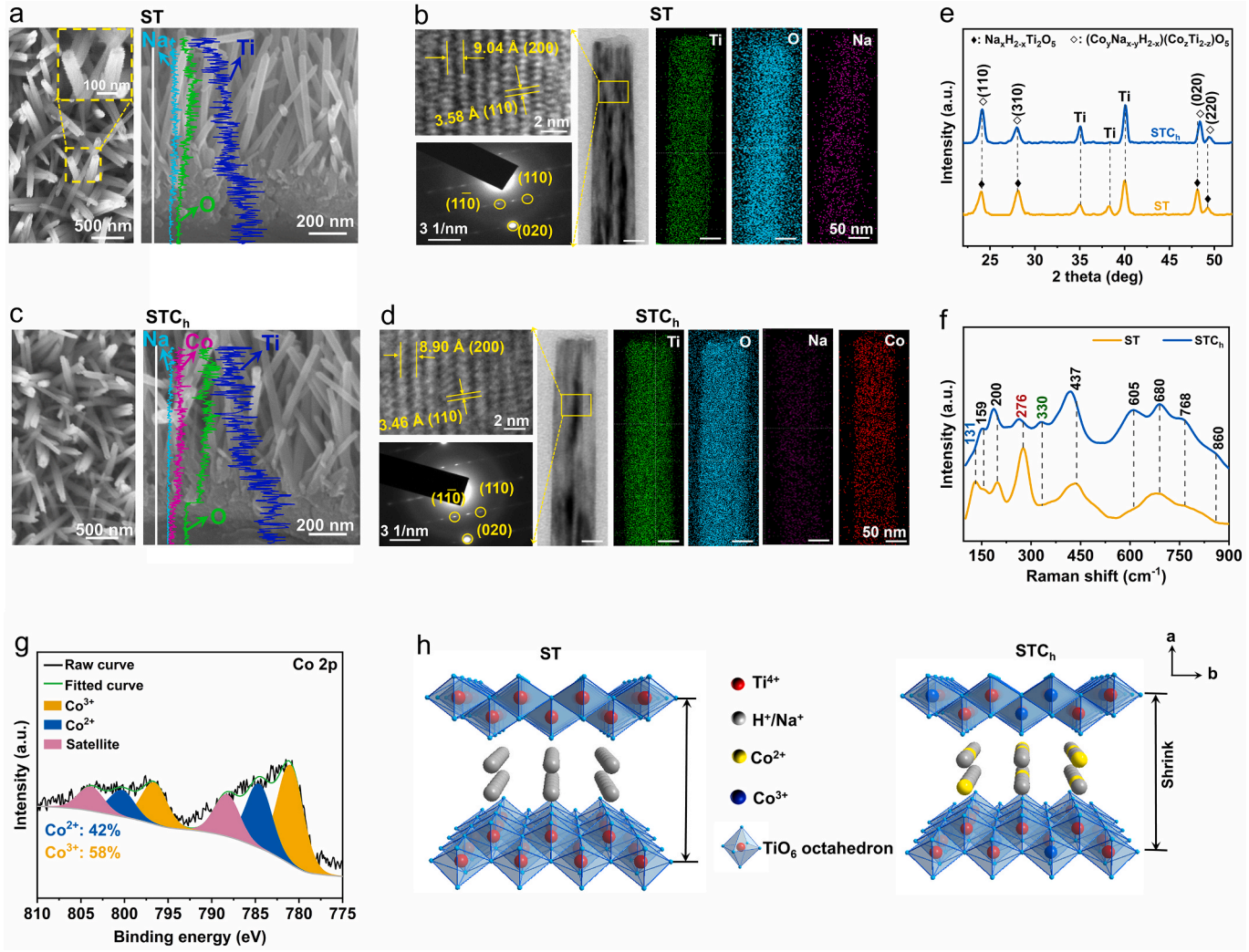

Fig. 1. Topographies and microstructures of ST and STC$_h$ arrays. SEM pictured surface and cross-sectional images of (a) ST and (c) STC$_h$ as well as elemental distribution profiles of Na, Ti, O and Co with different colors along the cross-sections. TEM panoramic bright-field and EDX mapping images of the nanorods picked up from (b) ST and (d) STC$_h$ as well as HRTEM images and SAED patterns from the yellow rectangle-marked regions on the nanorods. (e) XRD patterns of ST and STC$_h$. (f) Raman spectra of ST and STC$_h$. (g) High-resolution XPS spectra of Co 2p detected on STC$_h$ and corresponding atomic percents of Co^{2+} or Co^{3+} relative to total Co ions. (h) Schematic diagrams of atom stack models of ST and STC$_h$ along with their layered structures.

(CCR7) and Arg-1 stained respectively with anti-CCR7 and anti-Arg-1 antibodies (Servicebio) in infective case, EC indicatives CD31 and endomucin (Emcn) stained respectively with anti-CD31 and anti-Emcn antibodies (Servicebio), neuron indicative β-III-Tubulin stained with anti-β-III-Tubulin antibody (Servicebio), sensory neuron indicative SP stained with anti-SP antibody (Servicebio), sympathetic neuron indicative TH stained with anti-TH antibody (Servicebio), and cellular nuclei stained with DAPI (Servicebio) were conducted in normal cases. After that, the stained foils were observed using a Panoramic scanner (3D HISTECH, Hungary) and fluorescence intensities were analyzed using ImageJ software.

2.4.3. Osteogenic evaluations of the arrayed pillars

The pillars-contained femurs both in normal and infective cases retrieved post implantation of 6 weeks were examined for new bone formation using Micro-CT, push-out force examination, Van Gieson (VG), and polychrome sequential fluorescence staining, respectively, as demonstrated in details in **SI**.

2.5. Statistical analysis

The results were described as mean ± standard deviation (SD). The data were analyzed using SPSS software (USA) with one-way ANOVA method.

3. Results and discussion

3.1. Microstructure of the Co-doped nanorods-arrayed coatings on titanium substrates

Firm adhesion of coatings to metallic implants is necessary for their long-span service. However, the hydrothermally grown ST nanorods-arrayed coating usually displays a relatively weak adhesion to smooth Ti with a scratch-tested critical load (*Lc*) of 20.95 ± 0.91 N, as reported in our previous work [1]. To overcome the drawback, AE-derived coarsening of Ti discs was herein carried out prior to hydrothermal growth of ST coatings; with the optimized coarsening, i.e., AE of Ti for 5 min to set up the root-mean-square roughness (*Rq*) of 220 nm, the resultant ST coating exhibits the highest *Lc* of 43.40 ± 1.13 N, as described in SI and Fig. S1.

The hydrothermally grown ST nanorods-arrayed coating on the 5 min-AE-treated Ti is bilayer structured, comprising a thin layer of nanogranulates adjacent to Ti, and an overlapping layer of quasi-vertical nanorods with a diameter of 70.1 ± 2.5 nm, length of ~2 μm and

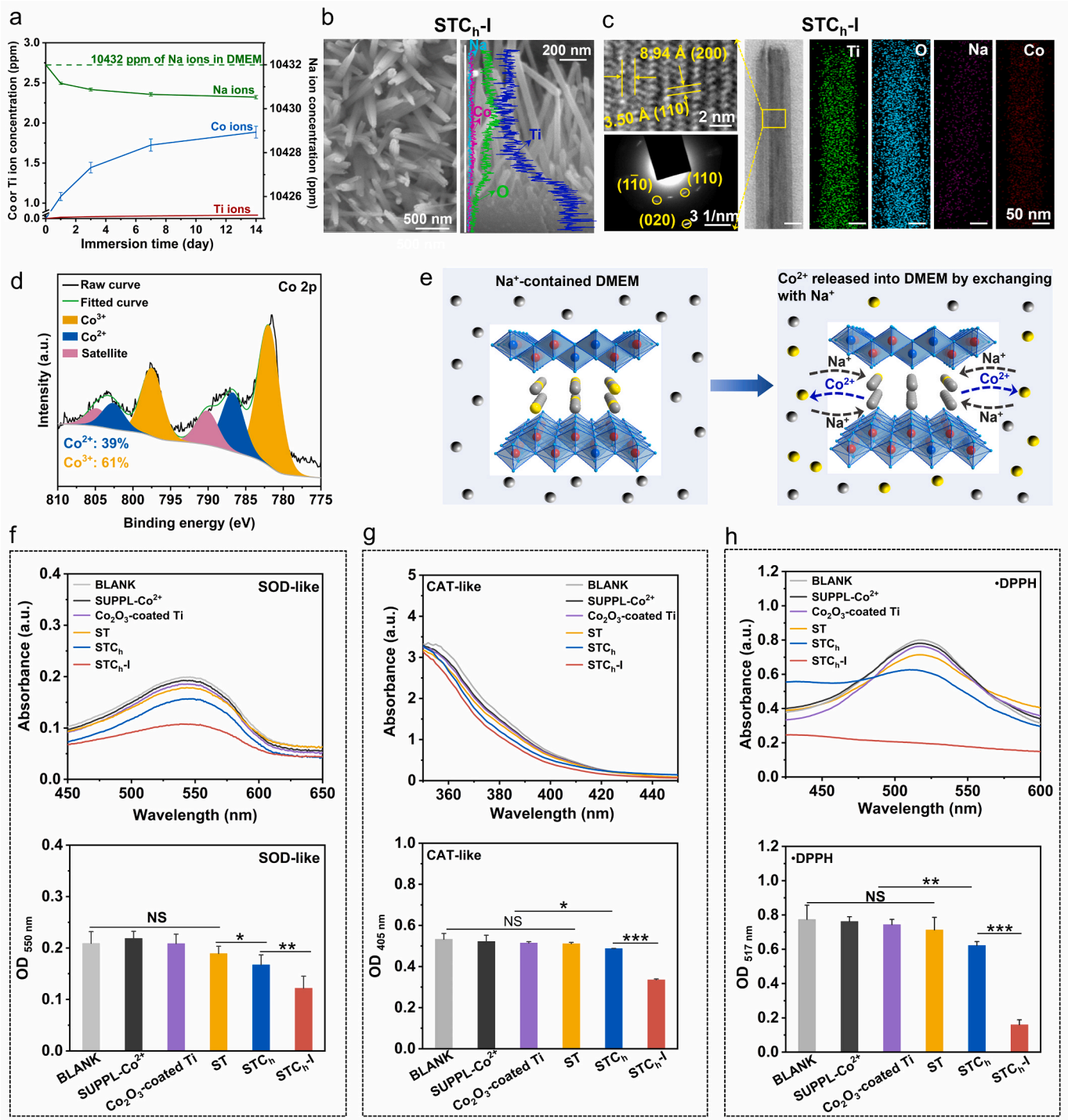

Fig. 2. Topographies and microstructures of STC$_h$-I as well as ionic release behaviors and ROS scavenging properties of the arrays. (a) Na, Co, and Ti ion concentration of DMEM immersing STC$_h$ array as a function of immersion time. (b) SEM pictured surface and cross-sectional images of STC$_h$-I (the resultant array that STC$_h$ array immersed in DMEM solution for 14 days) as well as elemental distribution profiles of Na, Ti, O and Co with different colors along the cross-section. (c) TEM panoramic bright-field and EDX mapping images of the nanorods picked up from STC$_h$-I as well as HRTEM image and SAED pattern from the yellow rectangle-marked region on the nanorod. (d) High-resolution XPS spectra of Co 2p detected on STC$_h$-I and corresponding percents of Co^{2+} or Co^{3+} relative to total Co ions. (e) Schematic diagram of Co^{2+} released from STC$_h$ into DMEM via exchanging with Na^+. (f) SOD-like activities of ST, STC$_h$, and STC$_h$-I for removal of $\bullet O_2^-$. (g) CAT-like properties of ST, STC$_h$, and STC$_h$-I for removal of H_2O_2. (h) DPPH assayed total ROS scavenging activities of ST, STC$_h$, and STC$_h$-I. BLANK: the plain test solutions; SUPPL-Co^{2+}: the test solutions supplemented with Co^{2+} in dose equal to that released from STC$_h$ for 14 days; data are presented as mean ± SD, $*p < 0.05$, $**p < 0.01$, $***p < 0.001$, and NS: no significance.

interrod spacing of 72.4 ± 3.2 nm (Scanning Electron Microscopy (SEM) images in Fig. 1a). This array consists of monoclinic ST with a formula of $Na_xH_{2-x}Ti_2O_5$ (Transmission Electron Microscopy (TEM) selected area electron diffraction (SAED) pattern in Fig. 1b and X-ray Diffraction (XRD) pattern in Fig. 1e), in which the individual nanorod stacks by TiO_6 octahedra in the radial direction, i.e., a-axis [200] and growing along the b-axis [020] (Fig. 1b).

Subsequently, the ST-arrayed Ti discs were mounted in autoclaves

containing aqueous solutions with Co^{2+} concentrations ($[Co^{2+}]_{as}$) of 0.05, 0.1, 10, and 50 mM, respectively, and hydrothermally doped at 100 °C for 2 h. All the resultant arrays keep unchangeable in morphology compared to the primitive one (Fig. S2), and the Co contents detected on the arrays-coated Ti discs by energy dispersive X-ray (EDX) tend to increase with $[Co^{2+}]_{as}$, reaching the highest dose at $[Co^{2+}]_{as}$ of 10 mM, without further increasing even at $[Co^{2+}]_{as}$ of 50 mM (the inserted data in Fig. S2). In details for the array hydrothermally doped at $[Co^{2+}]_{as}$ of 10 mM, namely STC_h, Co ions appear to incorporate into its nanorods in whole length uniformly (EDX elemental profiles in Fig. 1c, mapping images in Fig. 1d) with a doping dose of 7.7 ± 1.0 at% (Table S5). This incorporation leads to the decrease in Ti and Na contents without altering O content within the nanorods of STC_h (Table S5), suggesting that the doped Co ions substitute Ti ions partially and Na ions mostly, both of which are known to locate respectively within TiO_6 octahedra and at TiO_6 octahedral interlayers of ST lattice [42]. This viewpoint is supported by the evidence that the doping of Co ions does not alter phasic structure (XRD patterns in Fig. 1e and SAED patterns in Fig. 1b *vs* d), but results in right shift of XRD peaks (Fig. 1e) and decrease of interplanar spacings (high-resolution TEM (HRTEM) images in Fig. 1b *vs* d), owing to the radius of Co^{2+} (0.65 Å) [43] smaller than those of Ti^{4+} (0.68 Å) [1] and Na^+ (0.95 Å) [44]. To identify the doping sites of Co ions in STC_h more directly, Raman spectra were detected on STC_h and ST arrays as shown in Fig. 1f and the bond vibration modes corresponding to the Raman peaks are listed in Table S6. After Co doping, the vibration peak of Na–O bond locating at 131 cm^{-1} disappears while the vibration peak of the Na^+ -substituted ions locating at 330 cm^{-1} appears, indicating that Co ions are doped into TiO_6 octahedral interlayers; moreover, the stretching peak of Ti–O–Ti bond in TiO_6 octahedra, locating at 276 cm^{-1}, decreases and shifts towards left, indicating the substitute of Ti ions by Co ions.

Co ions are known to be changeable in valence state [40]. To identify their valence states, X-ray photoelectron spectroscopy (XPS) analyses were conducted (Fig. S3) and a Co 2p high-resolution XPS spectrum of STC_h array is shown in Fig. 1g. Clearly, STC_h contains both Co^{2+} and Co^{3+} with atomic percentages of 42 % and 58 % relative to total Co ions, as drawn according to that both kinds of the ions present binding energies at 796.04 and 780.55 eV [45] as well as at 800.10 and 785.12 eV [45], respectively. As known, there are two kinds of cationic doping sites in ST crystal lattice, i.e., octahedral interlayer for divalent cations such as Sr^{2+} [46], and Ti^{4+} position within TiO_6 octahedra for trivalent cations such as Eu^{3+} [43]. Also reportedly, when Fe^{2+} ions were doped in $Na_2Ti_3O_7$ to locate at Ti^{4+} sites, they would be compensated to a higher valence state Fe^{3+} according to the law of charge conservation [37]. It can be thereby deduced that the partial turnover of Co^{2+} to Co^{3+} in STC_h is due to the compensation effect of valence state for Ti^{4+}. Collectively, our results confirm that in STC_h, Co ions are doped at dual sites of the monoclinic lattice, i.e., in the form of Co^{2+} to locate at TiO_6 octahedral interlayers for substituting Na^+, and in the form of Co^{3+} to locate within TiO_6 octahedra for substituting Ti^{4+}, as schematically shown in Fig. 1h, endowing STC_h with a formula of $(Co_yNa_{x-y}H_{2-x})(Co_zTi_{2-z})O_5$. Notably, the incorporation of Co ions into STC_h array was evaluated to have no negative effect on its adhesion to Ti, with a *Lc* as high as 43.47 ± 1.11 N (Fig. S4).

3.2. Ionic release of STC_h array and its ROS scavenging capacity acting as nanoenzyme

By immersing the STC_h-arrayed discs in cell culture medium, DMEM, up to 14 days, the ionic concentrations of the resultant media were assessed as Fig. 2a. Visibly, the Ti ions released from STC_h are quite rare, but the Co ions released from STC_h are pronounced while the Na ion concentrations of the media decline with immersion, suggesting that STC_h array is insoluble in DMEM and its release of Co carries out via ionic exchange with Na in DMEM. Correspondingly, the immersed STC_h array in DMEM for 14 days, referred to as STC_h-I, does not exhibit any change in topography (Fig. 2b) and phase (Fig. S5 and SAED in Fig. 2c), but shows increased interplanar spacings and Na content as well as reduced Co content (HRTEM and elemental mapping images in Fig. 2c and Table S5) compared to STC_h. To identify which kind(s) of Co^{2+} and/or Co^{3+} to be released, XPS scan of Co 2p peak was reconducted on STC_h-I, showing that the atomic percentage of Co^{2+} relative to total Co ions decreases to 39 % while that of Co^{3+} increases to 61 % (Fig. 2d) compared to those of STC_h (Fig. 1g), indicating that the released Co ions are primarily Co^{2+} leading to an increased Co^{3+}/Co^{2+} atomic ratio in STC_h-I crystal lattice. Given that the Eu^{3+} doped within the TiO_6 octahedra of ST are hard to release owing to the high bond energy of Eu^{3+}-O [43], our results (Fig. 2a–d) indicate that the Co^{2+} doped at TiO_6 octahedral interlayers release out of STC_h lattice spontaneously via ionic exchange with Na^+ in DMEM while the Co^{3+} doped within TiO_6 octahedra release out hardly, as schematically shown in Fig. 2e. This exchange of Co^{2+} with Na^+ is deemed to be attributed to low bond energy of Co^{2+}-O relative to Co^{3+}-O [47] and to be derived by the Co^{2+}-induced high lattice distortion energy.

Prolonged excessive ROS in peri-implant milieu are known to sustain MΦs in M1 phenotype, harmful to osteogenesis, while native enzymes SOD and CAT scavenge $\bullet O^{2-}$ and H_2O_2, respectively [37]. Next, we examined the ROS-scavenging capacities of ST, STC_h and STC_h-I arrays, together with insoluble Co_2O_3-coated Ti, by immersing them in the test solutions of $\bullet O_2^-$-contained nitro blue tetrazolium formazan, H_2O_2-contained ammonium molybdate, and ethanolic DPPH (used for detecting total ROS including $\bullet O_2^-$, H_2O_2, $\bullet OH$, $^1O_2$, $\bullet O_2^{2-}$, etc.), respectively; also employing the plain test solutions (namely BLANKs), the test solutions supplemented with Co^{2+} in dose equal to that released from STC_h for 14 days (namely SUPPL-Co^{2+}) as controls. Notably, SUPPL-Co^{2+}, Co_2O_3 lattice-fixed Co^{3+} and ST array are shown to be solely lack of the ROS-scavenging capacity in details to remove $\bullet O^{2-}$ (Fig. 2f), H_2O_2 (Fig. 2g) and total ROS (Fig. 2h) compared with corresponding BLANKs. However, STC_h co-doped with Co^{2+} at octahedral interlayers and Co^{3+} within octahedra behaves as both SOD and CAT, exhibiting a considerable ROS-scavenging effect, and this effect is further enhanced with solution immersion as evidenced by STC_h-I (Fig. 2f–h), owing to the increased atomic ratio of Co^{3+} to Co^{2+} in the solution-immersed STC_h (e.g., STC_h-I) crystal lattice.

It is given that the Fe^{3+}-Fe^{2+} or Mn^{4+}-Mn^{2+} doped titanates and Ce^{4+}-Ce^{3+} doped titania act as SOD- and CAT-like enzymes, due to the strong charge transfer of these valence-mixed ion pairs [37–39]. Inspired by the catalytic equations of above mimetic enzymes, based on Fig. 2f–h depicted results, we deduce that our Co^{2+} and Co^{3+} co-doped STC_h array removes $\bullet O_2^-$ likely according to Equations (1) and (2), and removes H_2O_2 likely according to Equations (3) and (4), acting as a novel SOD- and CAT-like nanoenzyme for ROS scavenging.

$$\bullet O_2^- + 2Co^{3+} = 2Co^{2+} + O_2 + H^+ \quad (1)$$

$$2Co^{2+} + 2H^+ + O_2 = 2Co^{3+} + H_2O_2 \quad (2)$$

$$H_2O_2 + 2Co^{3+} + 2OH^- = 2Co^{2+} + 2H_2O + O_2 \quad (3)$$

$$H_2O_2 + 2Co^{2+} = 2Co^{3+} + 2OH^- \quad (4)$$

3.3. STC_h array-derived neural differentiation of MSCs

Co^{2+} ions are shown to have dose-dependent toxicity to bone-associated cells [41,48]. To this concern, we tested the cytocompatibility of STC_h array using BMSCs, MΦs and HUVECs, showing that STC_h array exhibits the viability and proliferation of these cells identical to TCP and pure Ti, and the dose of Co^{2+} ions released from STC_h array does not induce cytotoxicity to MΦs, BMSCs and HUVECs (Fig. S6).

To explore the effect of STC_h on BMSC differentiation into neuron or Schwann cell, BMSCs seeded on TCP and incubated in the culture medium supplemented with Co^{2+} in concentration identical to that released from STC_h at corresponding incubation time (namely TCP +

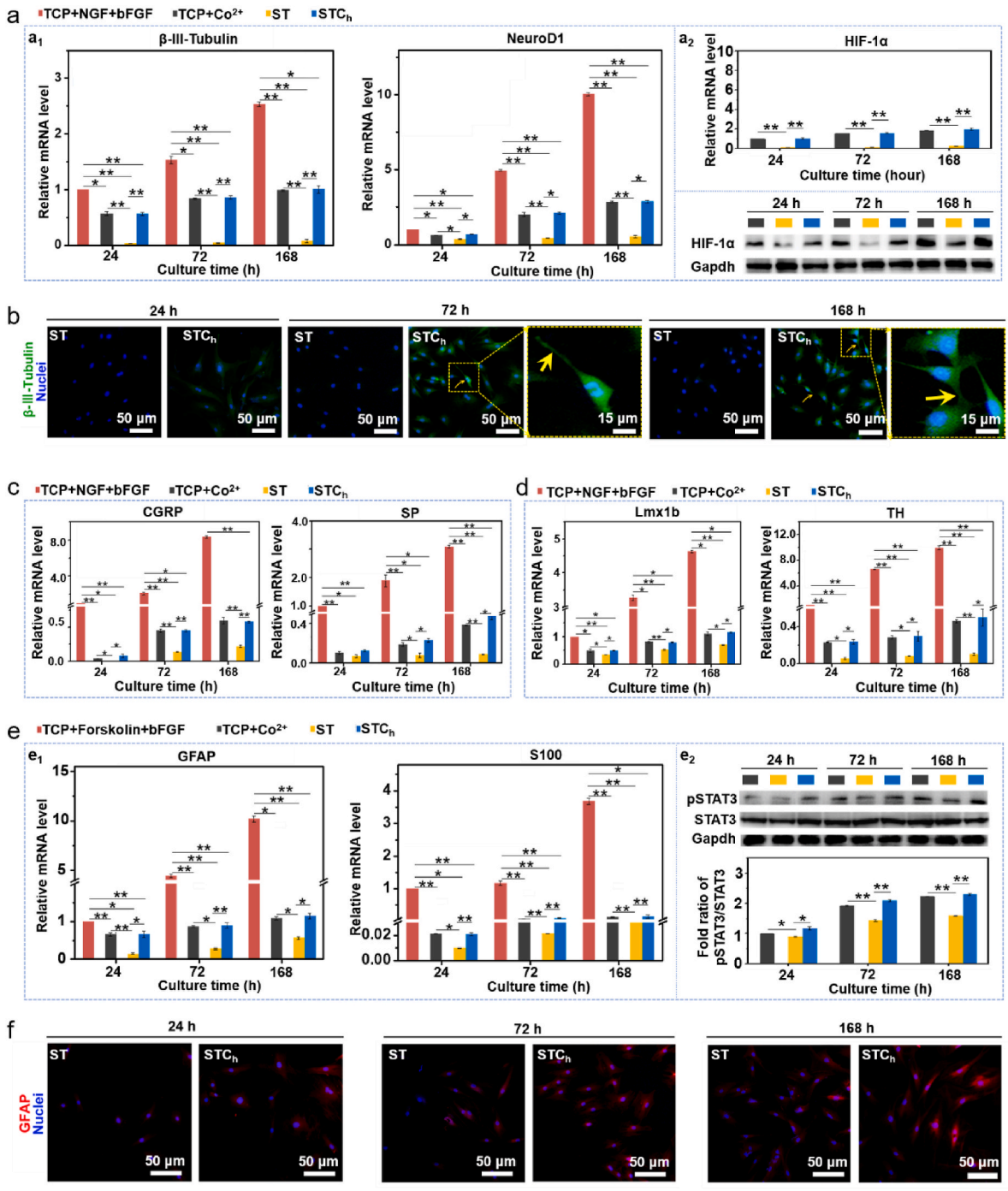

Fig. 3. Responses of the BMSCs seeded on ST and STC_h arrays at given culture time points. (a_1) mRNA expressions of β-III-Tubulin and NeuroD1 together with (a_2) mRNA and protein levels of transcriptional factor HIF-1α by the committed BMSCs. (b) Fluorescence staining images (merged) of β-III-Tubulin (green) and nuclei (blue) within the committed BMSCs (The yellow arrows marked the neuronal shape as featured by neurites). (c) CGRP and SP, (d) Lmx1b and TH, (e_1) GFAP and S100 mRNA expressions, together with (e_2) protein expressions of transcriptional factor STAT3, phosphoralyted STAT3 (pSTAT3) and the corresponding fold ratio of pSTAT3/STAT3 by the committed BMSCs. (f) Fluorescence staining images (merged) of GFAP (red) and nuclei (blue) within the committed BMSCs. Data are presented as mean ± SD, n = 3, $*p < 0.05$, $**p < 0.01$.

Co^{2+}) was selected as a control, together with BMSCs seeded on TCP and incubated in the culture medium supplemented with NGF and bFGF (namely TCP + NGF + bFGF) as a positive control for neuron [9] or forskolin and bFGF (namely TCP + Forskolin + bFGF) as a positive control for Schwann cell [49].

As shown in Fig. 3a_1, the BMSCs on TCP stimulated by NGF and bFGF highly express neuron specific markers β–III–Tubulin and NeuroD1 at mRNA level. Similarly, STC_h array elicits the BMSCs seeded on it to considerably express β–III–Tubulin and NeuroD1 higher than TCP + Co^{2+} and far higher than ST array at gene (Fig. 3a_1) and protein (Fig. 3b and S7a) levels. Moreover, the BMSCs cultured on STC_h for 72~168 h reveal neuronal shape as featured by neurites (arrows-marked), but nor do the BMSCs on ST (Fig. 3b). Next, we identified the type of neurons differentiated from BMSCs. The BMSCs on STC_h array are shown to differentiate into both sensory and sympathetic neurons over time, with markers CGRP and SP specific for sensory neurons (Fig. 3c) as well as TH

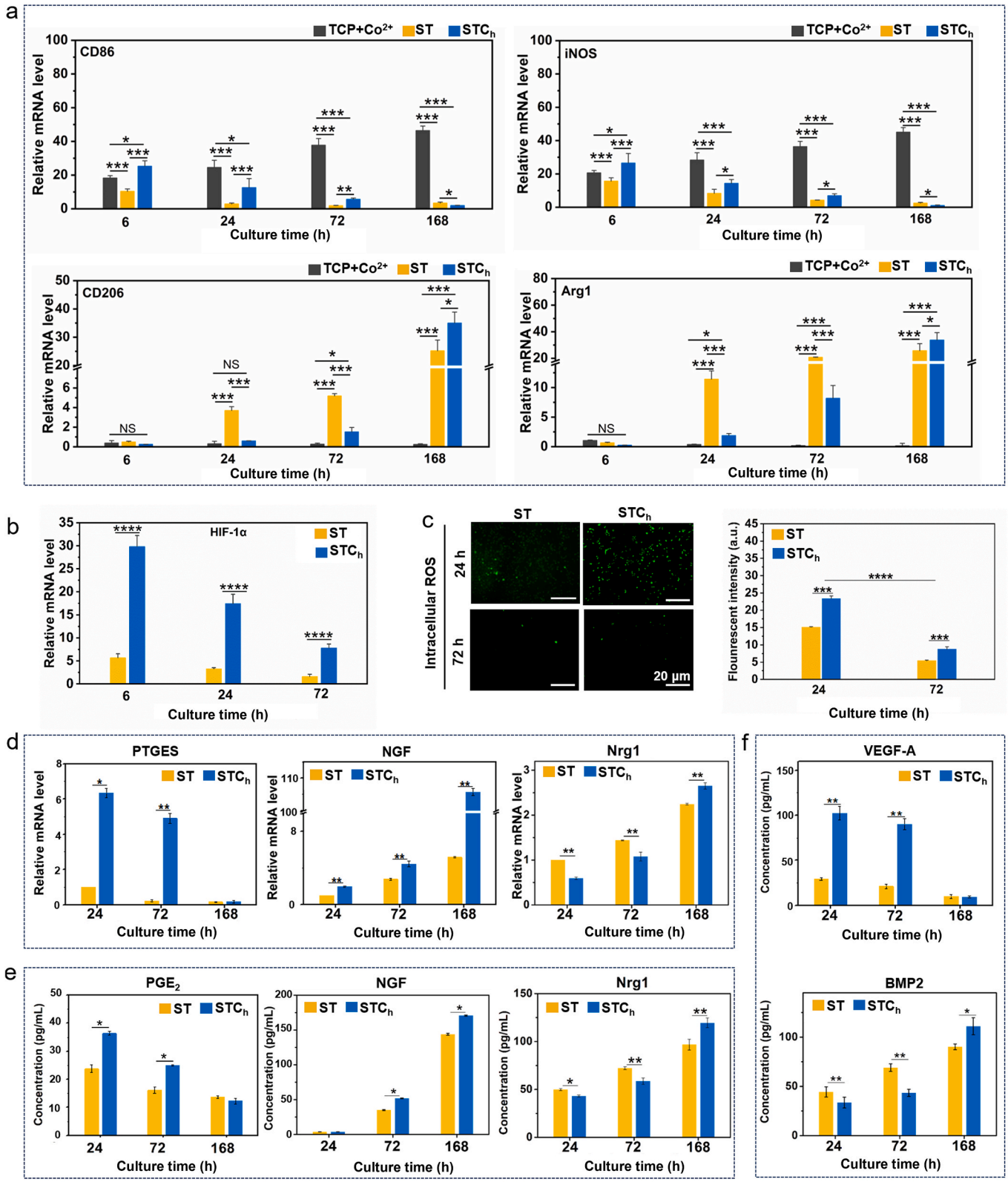

Fig. 4. Responses of the MΦs seeded on ST and STC_h arrays at given culture time points. (a) mRNA expressions of CD86 and iNOS as well as CD206 and Arg1 by the MΦs seeded on the arrays, together with on TCP + Co^{2+} as a control. (b) mRNA expressions of HIF-1α by the MΦs seeded on the arrays. (c) Intracellular ROS fluorescence staining images of the MΦs seeded on the arrays, and corresponding statistics of fluorescence intensities. (d) mRNA expressions of PTGES (synthase gene of PGE_2), NGF and Nrg1, secretions of (e) PGE_2, NGF and Nrg1 as well as (f) VEGF-A and BMP2 by the MΦs seeded on the arrays. Data are presented as mean ± SD, n = 3, $^*p < 0.05$, $^{**}p < 0.01$, and $^{***}p < 0.001$, $^{****}p < 0.0001$, and NS: no significance.

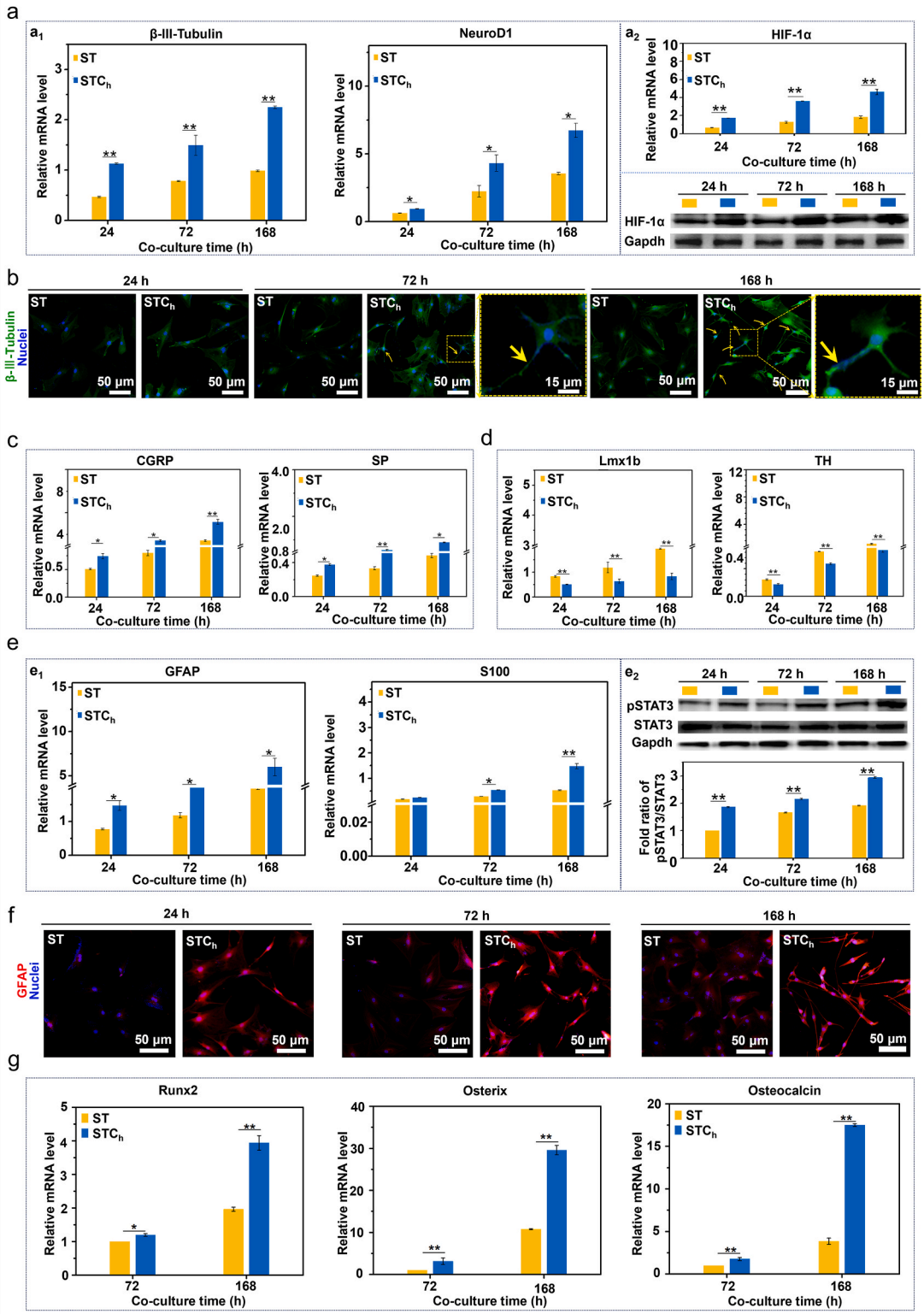

Fig. 5. Responses of the BMSCs seeded on transwell permeable membrane (TPM) to MΦs adhered on ST and STC_h arrays in co-culture model at given incubation time points. (a_1) mRNA expressions of β-III-Tubulin, NeuroD1 and (a_2) mRNA and protein levels of transcriptional factor HIF-1α by the BMSCs that were recruited onto TPM bottom side and then committed. (b) Fluorescence staining images (merged) of β-III-Tubulin (green) and nuclei (blue) within the committed BMSCs onto TPM bottom side (The yellow arrows marked the neuronal shape as featured by neurites). mRNA expressions of (c) CGRP and SP, (d) Lmx1b and TH, (e_1) GFAP, S100 and (e_2) protein expressions of pSTAT3 and transcriptional factor STAT3 together with corresponding fold ratios of pSTAT3 versus STAT3 by the committed BMSCs onto TPM bottom side. (f) Fluorescence staining images (merged) of GFAP (red) and nuclei (blue) within the committed BMSCs onto TPM bottom side. (g) mRNA expressions of Runx2, Osterix and Osteocalcin by the committed BMSCs onto TPM bottom side. Data are presented as mean ± SD, n = 3, $*p < 0.05$, $**p < 0.01$.

and Lmx1b specific for sympathetic neurons (Fig. 3d) lower than those expressed by TCP + NGF + bFGF-stimulated BMSCs, but higher than those expressed by TCP + Co^{2+}-stimulated BMSCs and far higher than those expressed by the BMSCs on ST array. These results indicate that STC_h array can directly stimulate differentiation of BMSCs into neurons, especially sensory and sympathetic neurons, ascribing to the dual stimuli of the released Co^{2+} predominantly and the nanotopographic effect quite weakly.

As shown in Fig. 3e_1, the BMSCs on TCP stimulated by forskolin and bFGF highly express Schwann cell specific markers GFAP and S100 at mRNA level. Likewise, STC_h array triggers the adhered BMSCs to apparently express these specific markers higher than TCP + Co^{2+} and much higher than ST array at mRNA (Fig. 3e_1) and protein (Fig. 3f and S7b) levels. Moreover, the BMSCs cultured on STC_h array for 24∼168 h gradually exhibit an elongated bipolar shape that is unique for Schwann cells [50], and this shape feature is much more visible than that of the BMSCs cultured on ST at each culture time (Fig. 3f). These results indicate that STC_h array can directly stimulate differentiation of BMSCs into Schwann cells, ascribing to the released Co^{2+} predominantly and the nanotopographic effect weakly. Notably, the nanorod-like topography plays a slightly obvious role in Schwann cellular differentiation relative to neuronal differentiation, in spite of the role being weak.

To clarify why STC_h array stimulates BMSCs to differentiate into both neurons and Schwann cells more pronouncedly than ST array, the transcriptional factors HIF-1α and STAT3 in the committed BMSCs on STC_h and ST were assayed. Visibly, STC_h array stimulate BMSCs to express HIF-1α at both gene and protein levels (Fig. 3a_2 and S8), pSTAT3 at protein level (Fig. 3e_2) higher than TCP + Co^{2+} and far higher than ST array. Highly expressed HIF-1α was reported to mediate the enhanced expression of miR-124a in BMSCs, which downregulates anti-neural small C-terminal phosphatase 1 (SCP1) and SRY-box transcription factor 9 (SOX9), promoting neuronal differentiation of BMSCs [51]. Concomitantly, HIF-1α encodes β–III–Tubulin [52] and NeuroD1 [53], leading to their expressions. Also, highly expressed pSTAT3 was proven to mediate the enhanced expression of miR-21 in MSCs, which downregulates SOX2, promoting MSCs to differentiate into Schwann cells [54]. Concomitantly, pSTAT3, SMAD1 and the transcriptional coactivator p300/CBP form a complex, inducing transcriptions and thereby expressions of GFAP and S100 [55]. Radically, cellular hypoxia mediates HIF-1α expression [56] and STAT3 phosphorylation [57], while Co^{2+} can incur cellular hypoxia [56]. Thus, our STC_h array can upregulate HIF-1α expression (Fig. 3a_2 and S8) and enhance STAT3 phosphorylation (Fig. 3e_2) via releasing Co^{2+} (Fig. 2a), deriving BMSCs to differentiate into neurons that express β–III–Tubulin and NeuroD1 (Fig. 3a_1), and Schwann cells that express GFAP and S100 (Fig. 3e_1), respectively.

3.4. STC_h array-derived macrophage responses

Based on the specific cytokines CD86/iNOS for M1 mark and CD206/Arg-1 for M2 mark [1], MΦ phenotype response to STC_h array was assayed along with ST array and TCP + Co^{2+} by qRT-PCR (Fig. 4a) and flow cytometry (Fig. S9). MΦs conditioned by TCP + Co^{2+}, i.e., seeded on TCP and stimulated by Co^{2+} with dose equal to that released from STC_h at corresponding culture time, express CD86 and iNOS highly but CD206 and Arg-1 rarely over culture of 6∼168 h, being pronouncedly polarized to M1 phenotype in a Co^{2+} dose-dependent manner. However, ST array triggers MΦs to express CD86 and iNOS visibly at 6 h but damply since 24 h, and so conversely do CD206 and Arg-1, indicating ST array induces MΦs in M1 response at 6 h and in M2 response since 24 h, owing to the physical stimulus of nanorod-like topography [1]. Compared to TCP + Co^{2+} and ST, STC_h array is evidenced to evoke the adhered MΦs in M1 response prior to 72 h and in M2 response thereafter (Fig. 4a and S9), which may be contributed to the nanorod-like topography, and overriding chemical stimuli of STC_h array-released Co^{2+} and -derived nanoenzyme effect.

Regarding the underlying mechanisms, besides the topographic effect of nanorods on MΦ phenotype as given in our previous work [1], the released Co^{2+} from STC_h was tested to evoke MΦs expressing the transcription factor HIF-1α more pronouncedly than ST array (Fig. 4b), while HIF-1α high expression is proven to elevate inducible NO synthase and thus induce M1 polarization of MΦs [58]. Moreover, STC_h array acts as SOD- and CAT-like enzyme with an extracellular ROS-scavenging effect, and the effect is gradually enhanced with immersion in media (Fig. 2f–h). This extracellular ROS-scavenging has been demonstrated to activate the transcription factor STAT6 of MΦs, mediating their polarization towards M2 phenotype [59]. Given M1 MΦs intrinsically revealing a high level of intracellular ROS in contrast to M2 MΦs [60], the examined result that the intracellular ROS level of MΦs on STC_h array appears pronounced at 24 h and attenuated at 72 h with level as low to undetectable as that of MΦs on ST (Fig. 4c), further supports the role of STC_h array as a nanoenzyme in the regulation of M1-to-M2 phenotype transition.

Given the role of PGE_2/NGF in promoting neuronal [30–32] and NGF/Nrg1 in boosting Schwann cellular [16,36] differentiation of BMSCs, the secretion profiles of these neurogenic factors by MΦs seeded on STC_h array were examined. STC_h array triggers MΦs to more pronouncedly express PTGES (synthase gene of PGE_2) and NGF (Fig. 4d) and secrete PGE_2 and NGF compared to ST array (Fig. 4e), with secretion declining for PGE_2 and enhancing for NGF over culture time of 24∼168 h. Moreover, Nrg1 secretions by MΦs on STC_h and ST arrays tend to increase (Fig. 4e) following its expressions (Fig. 4d) with culture; however, post 72 h, STC_h elicits MΦs to secrete more Nrg1 than ST. In combination of Fig. 4a with e, it is indicated that STC_h array can stimulates MΦs to considerably secrete neurogenic factors PGE_2, NGF and Nrg1 in a MΦ phenotype-dependent manner, consistent with elsewhere reported — M1 MΦs secreting PGE_2 and NGF [24–26,61], M2 MΦs secreting NGF and Nrg1 [24,25,33]. In addition, STC_h array was also detected to trigger MΦs to secrete angiogenic factor VEGF-A and osteogenic factor BMP2 in a MΦ phenotype-dependent manner, i.e. M1 MΦs secreting VEGF-A and M2 MΦs secreting BMP2 (Fig. 4f), consistent with the finding drawn on ST array in our previous work [1].

3.5. Neural and osteogenic differentiation of MSCs derived by STC_h array released Co^{2+} and conditioned MΦs in vitro

Inspired by our result that STC_h array can stimulate differentiation of BMSCs into neurons (Fig. 3a_1) and Schwann cells (Fig. 3e_1) predominantly via releasing Co^{2+} but also stimulate MΦs to secrete neurogenic factors PGE_2, NGF and Nrg1 (Fig. 4e), we further assayed the neurogenic responses of BMSCs to both STC_h-released Co^{2+} and the neurogenic factors secreted by STC_h-conditioned MΦs via transwell co-culture model (i.e., BMSCs co-cultured with MΦs seeded on the arrayed discs, schematically as Fig. S10). In terms of β–III–Tubulin and NeuroD1 expressions at gene (Fig. 5a_1) and protein (Fig. 5b and S11a) levels as well as neurites-featured cellular shape, STC_h array exhibits a higher ability to promote neuronal differentiation of BMSCs than ST array in the co-culture model. Notably, both the arrays evoke BMSCs to differentiate into neurons more pronouncedly in the co-culture case compare to the mono-culture case (Fig. 3a_1 and b). Regarding the neuronal type, based on the gene expressions of CGRP/SP (Fig. 5c) and TH/Lmx1b (Fig. 5d), BMSCs are derived to differentiate into more sensory neurons by both STC_h and ST arrays, and more sympathetic neurons by ST array in the co-culture case compare to the mono-culture case (Fig. 3c and d). In the co-culture model, however, STC_h array renders BMSCs to differentiate into more sensory neurons but less sympathetic neurons than ST array. In light of GFAP and S100 expressions at mRNA (Fig. 5e_1) and protein (Fig. 5f and S11b) levels as well as elongated bipolar shape, STC_h array is shown to also promote differentiation of BMSCs into Schwann cells more obviously compare to ST array in the co-culture case, and both the arrays evoke BMSCs to differentiate into Schwann cells more pronouncedly in the co-culture case compare to the mono-culture case (Fig. 3e_1 and f).

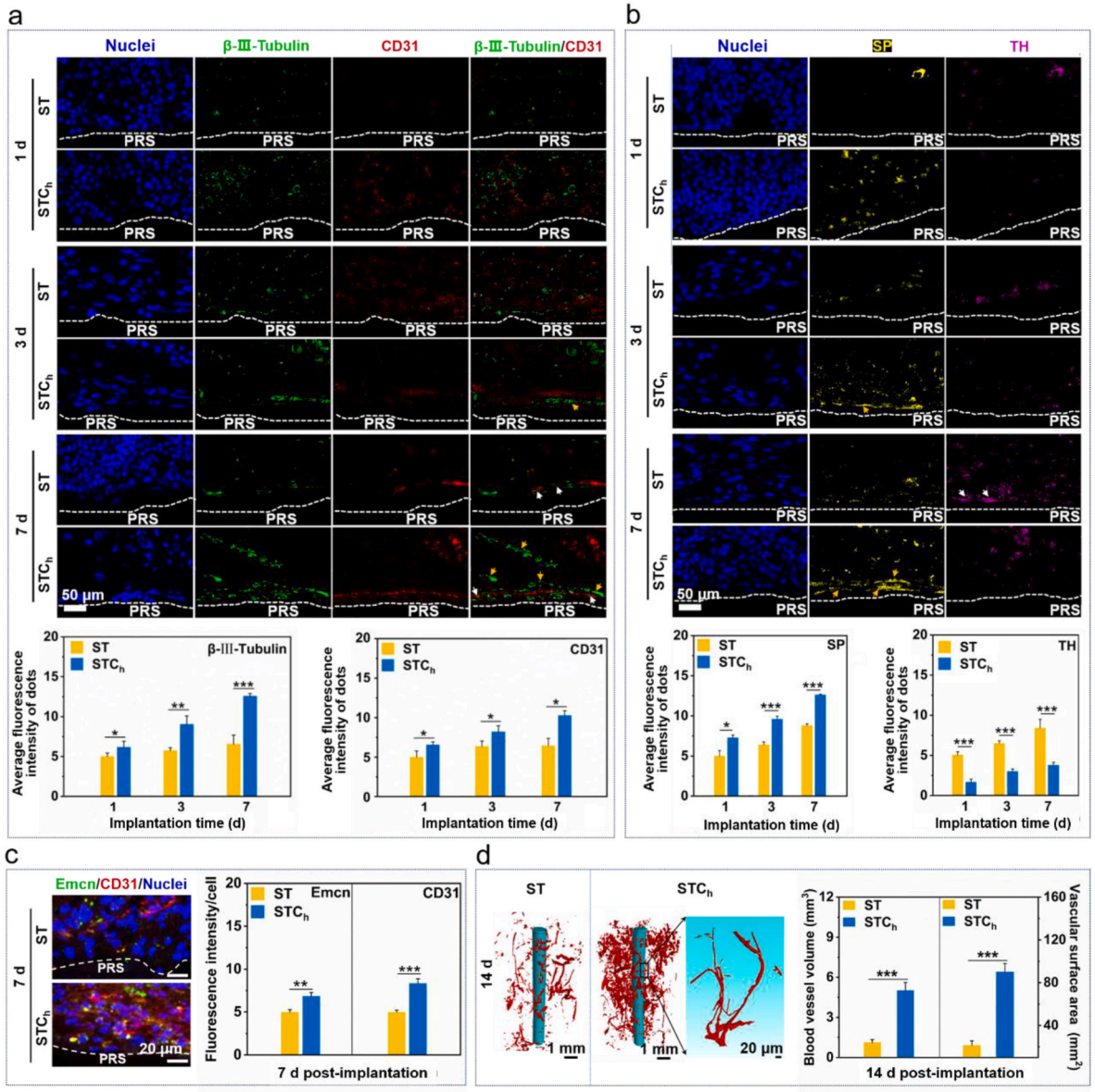

Fig. 6. Characterization of nerve fibers and blood vessels within the tissues surrounding the ST and STC_h arrayed pillars implanted in rat bone marrow. Fluorescent staining of (a) nuclei (blue), β-III-Tubulin (green) and CD31 (red) adjacent to PRS at 1, 3, and 7 d of implantation as well as quantified fluorescence intensities. Yellow and white arrows indicate sensory nerve fibers and vessels, respectively. (b) nuclei (blue), SP (yellow), TH (pink) adjacent to PRS at 1, 3, and 7 d of implantation as well as quantified fluorescence intensities. Yellow and white arrows indicate sensory nerve fibers and sympathetic nerve fibers, respectively. (c) Fluorescent staining images (merged) of nuclei (blue) as well as CD31 (red) and Emcn (green) marked vessels adjacent to PRS at 7 d, together with quantified fluorescence intensities of CD31 and Emcn. (d) Micro-CT reconstructed 3D angiography images of capillaries around ST and STC_h coated pillars at 14 d post-implantation, and quantitation of vascular volume and vascular surface area. Data are presented as mean ± SD, n = 4, $*p < 0.05$, $**p < 0.01$, $***p < 0.001$.

These results indicate a much stronger role of the neurogenic factors secreted by STC_h-conditioned MΦs than the STC_h-released Co^{2+} in promoting neuronal and Schwann cellular differentiation of BMSCs. Thereby, the expected strategy that promote neural differentiation of MSCs without loading exogenous neurotrophins in implants for nerve regeneration, may be feasible via modulating endogenous MΦs by STC_h-arrayed implants.

To clarify why STC_h array promotes neural differentiation more strongly in the co-culture case, the gene and protein expressions of transcriptional factors HIF-1α and STAT3 in the committed BMSCs were assayed as Fig. 5a_2, **S12**, and **5**e_2. As known, STC_h array can stimulate MΦs to secrete neurogenic factors PGE_2, NGF and Nrg1 (Fig. 4e). Besides STC_h-released Co^{2+}, PGE_2 and NGF were reported to individually enhance HIF-1α expression via the PGE_2 receptor 2 (EP2)-dependent pathway [62,63] and NGF-TrkA pathway [64], respectively; their synergistic actions induce BMSCs to more strongly express HIF-1α in the co-culture case (Fig. 5a_2 and **S12**) compare to the mono-culture case (Fig. 3a_2 and S8), and consequently promote neuronal differentiation via miR-124a/SCP1/SOX9 pathway [51] as mentioned in **Section 3.3**. Different from NGF that was reported to promote differentiation of MSCs into both sensory and sympathetic neurons [2], PGE_2 was demonstrated to promote differentiation of MSCs into sensory neurons but inhibit their differentiation into sympathetic neurons both through the PGE_2 receptor 4 (EP4)-CREB pathway [61,65,66]. Also, Nrg1 was demonstrated to inhibit differentiation of MSCs into sympathetic neurons through downregulating TH, given that TH could mediate sympathetic neurons from MSCs through activating the ERK/JNK pathway [67]. As shown in Fig. 4e, STC_h array triggers MΦs to secrete more PGE_2 and NGF compared to ST array from 24 to 72 h, while post 72 h STC_h elicits MΦs to secrete more NGF and Nrg1 than ST in spite of the declined secretion

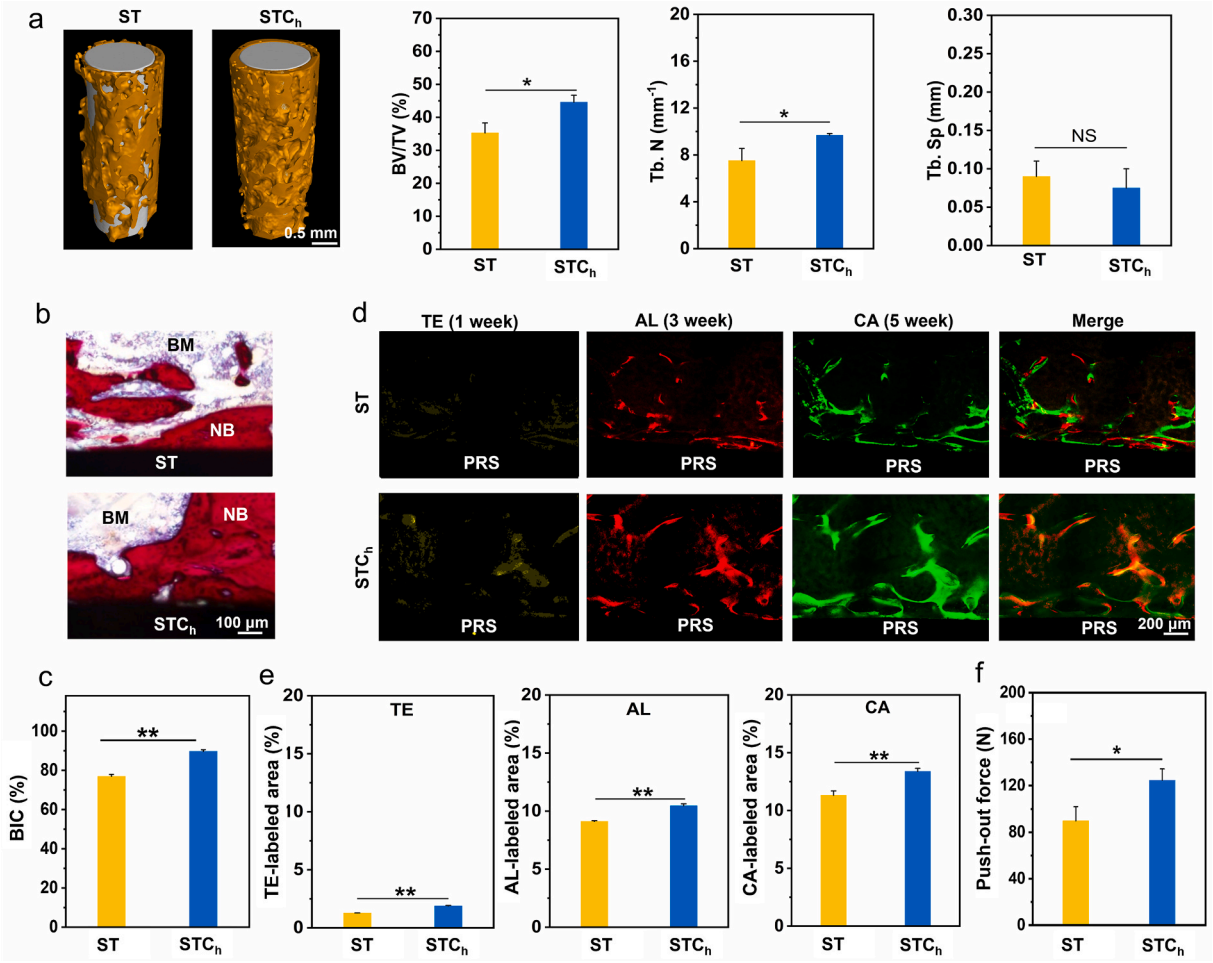

Fig. 7. Characterization of newly formed bone surrounding ST and STC_h arrayed pillars implanted in rat bone marrow for 6 weeks. (a) Micro-CT reconstructed images of newly formed bone around the pillars, and corresponding quantification of BV/TV, Tb. N and Tb. Sp. (b) VG staining images of newly formed bone surrounding the pillars (BM: bone marrow; NB: newly formed bone). (c) Statistics of BIC ratios based on (b). (d) Polychrome sequential fluorescent labeling images to show the formation process of new bone around the pillars: TE-labeled early Ca^{2+}-rich matrix, AL-labeled ensuring amorphous mineral, and CA-labeled subsequently crystallized mineral, together with (e) statistics of TE-, AL- and CA-labeled fluorescence areas, respectively. (f) Push-out forces of the arrayed pillars. Data are presented as mean ± SD, n = 6, $*p < 0.05$, $**p < 0.01$, and NS: no significance.

of PGE_2. The temporally enhanced secretions of PGE_2 and Nrg1, overlapping the sustained enhanced secretion of NGF, by STC_h-conditioned MΦs compared to ST-conditioned MΦs, result in STC_h array to promote BMSCs to differentiate into more sensory neurons but less sympathetic neurons than ST array in the co-culture case. On the other hand, NGF and Nrg1 were reported to individually induce pSTAT3 activation [68,69], consequently their synergistic actions induce BMSCs to more strongly enhance pSTAT3 expressions in the co-culture case (Fig. 5e$_2$) compare to the mono-culture case (Fig. 3e$_2$), and thus promote Schwann cellular differentiation via miR-21/SOX2 pathway [54] as mentioned in **Section 3.3**.

Also, we assayed the action of STC_h array on osteogenic differentiation of BMSCs in the co-culture model along with ST array. In light of the mRNA expressions of Runx2, Osterix and Osteocalcin in the committed BMSCs (Fig. 5g), STC_h array is shown to foster osteoblastic differentiation of BMSCs compared to ST array. Reportedly, Co^{2+} in the concentration range of 1~5 ppm could promote osteogenic differentiation of MSCs [41], and so did MΦs-secreted cytokines such as PGE_2, NGF, VEGF-A and BMP2 [1,4,6,7]. Correspondingly, our results show that the STC_h-released Co^{2+} concentrations at the given time points (Fig. 2a) fall in this range, and STC_h array-conditioned MΦs secrete a totally higher amount of cocktail containing PGE_2, NGF, VEGF-A and BMP2 than ST array-conditioned MΦs (Fig. 4e and f), which lead to the enhanced osteoblastic differentiation of BMSCs as derived by STC_h array compared to ST array in the co-culture model.

3.6. *In vivo neural network reconstruction, type-H capillary formation and bone-implant integration of STC_h-arrayed pillar*

STC_h and ST arrayed pillars were implanted in the femoral marrow cavities of S-D rats for a series of periods to assay the cellular responses, formation of nerve fibers and blood vessels within the temporary tissues around the pillars and subsequent *de novo* bone apposition on the pillars. It is known that β-III-Tubulin specifically stems from neuron distributing over its sphere-like cell body and fibrous neurites [3], while CD31 specifically stems from ECs [70]. At early stage post-implantation of the pillars, the immunofluorescence staining images of β-III-Tubulin, CD31 and DAPI-stained nuclei within the tissue sections adjacent to PRS are shown in Fig. 6a. On day 1, around ST array although a number of diverse cells appear, β-III-Tubulin green dots are weak in fluorescence intensity and spare, while CD31 red dots are almost invisible; around STC_h array, however, both β-III-Tubulin and CD31 dots increase in intensity and number compared with those around ST array. This result indicates that neurons appear prior to ECs, and STC_h array display a much stronger role in promoting neuronal differentiation of endosseous BMSCs than ST. With extending implantation to day 3 and further to day 7, β-III-Tubulin and CD31 dots around both ST and STC_h become pronounced and then gradually arrange in fiber/belt, respectively,

indicating the gradual formation of nerve fibers and later capillaries. Notably on day 7, the nerve fibers display two spatial orientations relative to capillaries. In details, a more part of nerve fibers parallel to capillaries (yellow-arrow marked) and a few parts of nerve fibers intertwining capillaries (white-arrow marked) present around STC_h array, while nerve fibers with opposite parts present around ST array. To identify neuronal type, we further stained sensory neuron-specific marker SP, and sympathetic neuron-specific TH in the tissue sections adjacent to PRS, as shown in Fig. 6b. Clearly, from day 1 to day 7 of implantation, SP yellow dots and TH pink dots around both ST and STC_h arrays become pronounced in intensity and number; however, STC_h array gives raise to the surrounding nerves with more sensory type than sympathetic type, while ST array renders the surrounding nerves with more sympathetic type than sensory type. In combination of Fig. 6a with b, it is suggested that sensory nerve fibers are parallel to and sympathetic nerve fibers wrap capillaries, consistent with the spatial orientations between nerves and blood vessels reported elsewhere [3,4]. Collectively, compared with ST array, STC_h array displays a much stronger role in promoting neurogenesis, with more sensory type than sympathetic type; it also promotes angiogenesis both *in vitro* and *in vivo* (Fig. S13, CD31-stained images of Fig. 6a on day 7). In particular the formation of type-H capillaries as identified by high expressions of both CD31 and Emcn (Figs. S13b, e, and f as well as Fig. 6c taken on day 7). Panoramically, the peri-implant capillaries are much pronounced for STC_h-arrayed pillar compared to ST-arrayed pillar (Fig. 6d taken on day 14).

Next, we examined the osteogenic ability of STC_h-arrayed pillar at week 6 together with ST-arrayed pillar. Micro-CT images show that STC_h induces more pronounced new bone formation compared to ST, validated by the quantitation of bone volume/total volume (BV/TV), trabecular number (Tb. N), and trabecular separation (Tb. Sp) within the ring region of 50 μm in width around the pillars (Fig. 7a). VG staining images demonstrate that STC_h induces a thicker layer of new bone to deposit directly on its surface with a bone-to-implant contact (BIC) ratio compared to ST (Fig. 7b and c), indicating an improved osseointegration of STC_h. Furthermore, the formation process of new bone around STC_h- and ST-arrayed pillars was demonstrated by labeling the bone matrix sequentially with tetracycline hydrochloride (TE) at week 1, Alizarin red S (AL) at week 3 and calcein (CA) at week 5. In general, following the secretion of collagen fibrils by osteoblasts, bone matrix mineralization undergoes a series of steps: initial formation of amorphous Ca–P complexes that can be labeled by TE [71], subsequent crystallization of the amorphous Ca–P complexes into small-sized and low-ordered apatite crystals which can be labeled by AL [72], and then fusing to large-sized and high-ordered apatite crystal plates which can be labeled by CA [73]. Furthermore, the push-out force of STC_h-arrayed pillar is ~120 N, 1.3 times greater than that of ST-arrayed pillar (Fig. 7f). Taken together, as confirmed by Fig. 7d, e and f, STC_h significantly accelerates the mineralization of its surrounding newly formed bone matrix at each of the steps, and promotes the formation of mineralized bone matrix compared to ST.

On the advantage of STC_h-derived peri-pillar tissues and osseointegration over those derived by ST, we present discussions as follows. Osseointegration of implants is known to be formed via inducing *de novo* bone apposition on their surfaces [1]. The *de novo* bone formation not only involves the interactions of cells such as MΦs, MSCs and ECs in order [1], but also is recently found to be innervated by endosseous sensory and sympathetic nerves as essential upstream regulators of vascularization and osteogenesis [2,6]. Our results show that in a stimulated body fluid (such as DMEM), Co^{2+} and Co^{3+} co-doped STC_h array, on one hand spontaneously releases Co^{2+} out of its lattice and detains Co^{3+} within its lattice (Fig. 2a–e), on the other hand acts as a nanoenzyme to scavenge ROS, and this ROS scavenging effect is further enhanced with immersion (Fig. 2f–h) owing to the increased Co^{3+}/Co^{2+} ratio in its resultant lattice. Via releasing Co^{2+}, STC_h array is shown to upregulate HIF-1α expression (Fig. 3a_2) and enhance STAT3 phosphorylation (Fig. 3e_2), deriving BMSCs to differentiate into neurons (Fig. 3a_1 and b) and Schwann cells (Fig. 3e_1 and f), respectively. Furthermore, contributed to the overriding chemical stimuli of the released Co^{2+} and later the nanoenzyme-derived ROS scavenging, STC_h array is shown to evoke MΦs in M1 response prior to 72 h and in M2 response thereafter (Fig. 4a), while ST array induces MΦs in M1 response at 6 h and in M2 response since 24 h owing to the physical stimulus of nanorod-like topography. The arrays-conditioned MΦs were observed to considerably secrete neurogenic factors PGE_2, NGF and Nrg1 as well as angiogenic VEGF-A and osteogenic BMP2 in a MΦ phenotype-dependent manner, i.e., M1 cells secrete PGE_2, NGF and VEGF-A while M2 cells secrete NGF, Nrg1 and BMP2 (Fig. 4a–e, f). Under the synergistic actions of STC_h-released Co^{2+} and the neurogenic factors secreted by STC_h-conditioned MΦs *in vitro*, STC_h array is shown to promote neuronal (Fig. 5a_1 and b) and Schwann cellular (Fig. 5e_1 and f) differentiation of BMSCs more pronouncedly compared to ST array; in particular, STC_h array renders BMSCs to differentiate into more sensory neurons (Fig. 5c) but less sympathetic neurons (Fig. 5d) than ST array. This *in vitro* result on neural differentiation of BMSCs is in agreement with and account for the endosseous neuronal differentiation of MSCs and subsequent formation of nerve fibers (Fig. 6a), and in particular the *in vivo* result that STC_h array gives raise to the surrounding nerves with more sensory type than sympathetic type and so conversely does ST array (Fig. 6b). Reportedly, Co^{2+} could promote the expression of HIF-1α and its downstream VEGF-A in ECs, promoting angiogenesis [56]. M1 MΦs-secreted PGE_2 [28], VEGF-A [56] and M2 MΦs-secreted BMP2 [1] could promote angiogenesis. Most Importantly, early regenerated nerves-secreted CGRP and SP are given to promote angiogenesis [4,5]; in particular, CGRP has been recently found to promote the formation of type H vessels [74]. Benefiting from the synergistic effects of Co^{2+} and the aforementioned inducible factors, the capillaries and in particular type-H capillaries stimulated by STC_h array are enhanced both *in vitro* (Fig. S13) and *in vivo* (Fig. 6c and d). Regarding osteogenesis, besides Co^{2+} [41] and MΦs-secreted cytokines PGE_2, NGF, VEGF-A and BMP2 [1,4,6,22,25], sensory nerve-secreted CGRP, SP and NGF [2,4,6] as well as sympathetic nerve-secreted VIP [2] were also reported to play important promoting roles. These cues derived by STC_h array lead to the enhanced osteoblastic differentiation of BMSCs (Fig. 5g) as mentioned in **Section 2.5**, which in combination with the type-H capillaries that further secrete pro-osteogenic factors such as VEGF-A and BMP2 [1], orchestrate the consequent new bone formation and osseointegration to be more pronouncedly enhanced around STC_h-arrayed pillar compared to ST-arrayed pillar (Section 3.5).

3.7. Phagocytosis of the arrays-conditioned MΦs on S. aureus in vitro and in vivo

Bacterial infection occurs frequently during implantation, leading to osteomyelitis and serious consequences, thereby implants are required to have a direct (e.g., loading antibacterial ions) or immune bacteria-killing activity at early stage [75]. Given that Co^{2+} has a dose-dependent bacteria-killing ability [76], we assayed the bacteria on Ti incubated in DMEM supplemented with Co^{2+} in dose equal to that released from STC_h on day 1 (1.08 ppm, Fig. 2a), along with bacteria on Ti incubated in DMEM, using Spread plate method (SPM). Notably, the viable bacteria in both cases are similar in number (Fig. S14), which is attributed to the fact that the Co^{2+} released from the array fell significantly below the minimum bacterial concentration of Co^{2+} (400 ppm) [77], excluding the contribution of the Co^{2+} dose released from STC_h to antibacterial function. Alternatively, MΦs are known to be able to clear bacteria via phagocytosing in M1 phenotype but lack of the ability in M2 phenotype [75]. To this end, the phagocytosis of *S. aureus* by the arrays-conditioned MΦs was assayed *in vitro*, using SPM via culture of the *S. aureus* phagocytosed in the MΦs conditioned by ST and STC_h, along with culture of the *S. aureus* phagocytosed in the MΦs conditioned by ST supplemented with LPS (namely ST + LPS) and ST supplemented

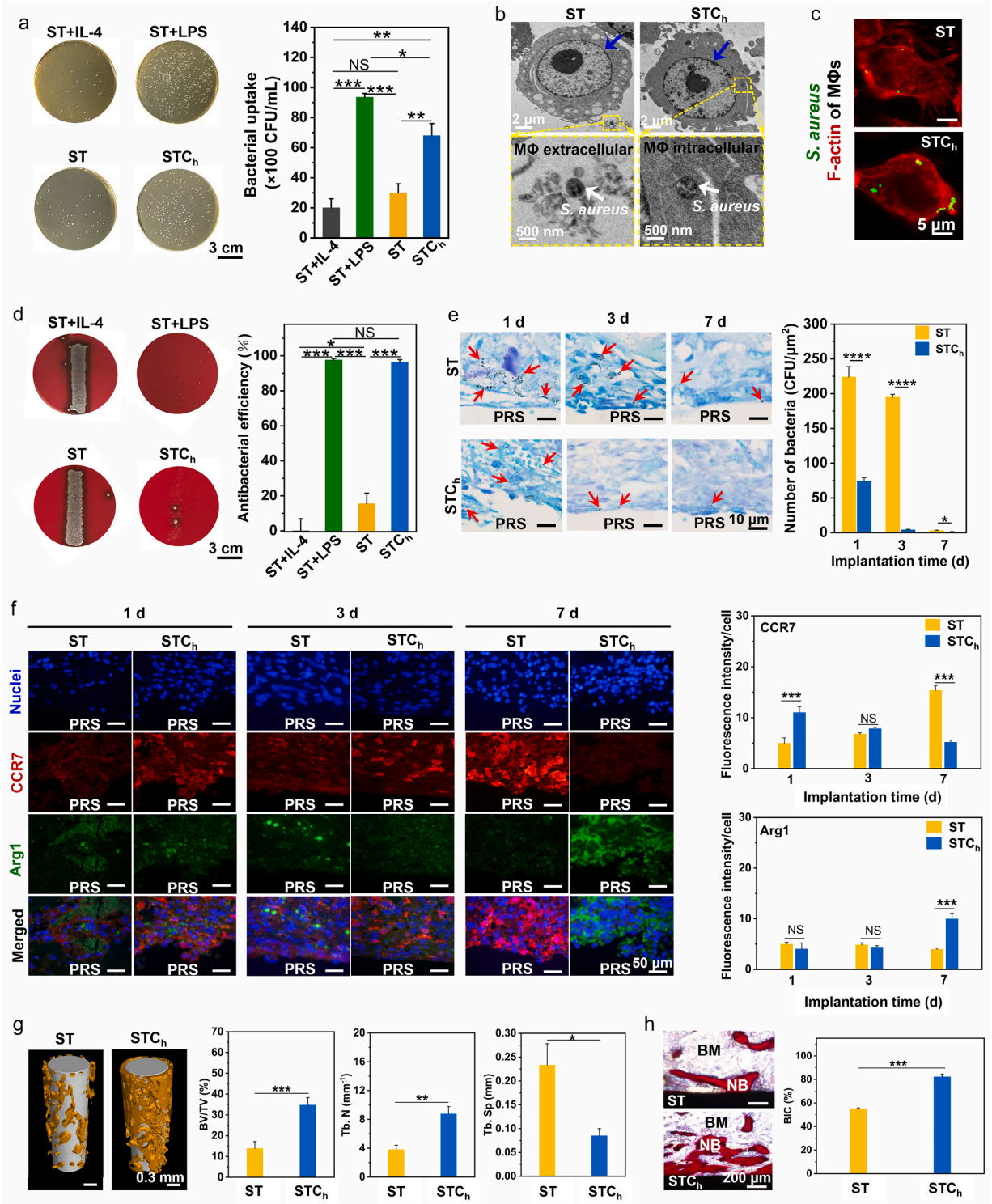

Fig. 8. ***In vitro* and *in vivo* phagocytosis of *S. aureus* by the arrays-conditioned MΦs, and formation of new bone surrounding ST and STC_h arrayed pillars in *S. aureus*-infected rat bone marrow.** (a) Optic photographs and statistics of bacterial colonies on agar plates, obtained from culture of the *S. aureus* phagocytosed in the MΦs conditioned by ST and STC_h along with ST + LPS (positive control) and ST + IL-4 (negative control) for 24 h. (b) TEM and (c) fluorescence staining images of the arrays-conditioned MΦs containing bacteria; in (b), blue and white arrows indicating MΦ nuclei and bacteria, respectively; in (c), MΦ F-actin being stained in red and *S. aureus* being stained in green. (d) Optic photographs of *S. aureus* colonies by rolling the 3 days-implanted ST and STC_h coated pillars on blood agar plates and re-culturing for 24 h, together with the corresponding antibacterial rates; ST + LPS and ST + IL-4, i.e., ST-coated pillars being inserted into rat femoral shafts followed by injection of PBS containing LPS and IL-4, respectively. (e) Giemsa staining images of peri-implant tissues at days 1, 3, and 7 of implantation (red arrows indicating bacteria), and quantification of bacteria within the tissues. (f) Fluorescent staining images of nuclei (blue), Arg1 (green), and CCR7 (red) adjacent to PRS, together with the corresponding quantified fluorescence intensities of Arg1 and CCR7. (g) Micro-CT reconstructed images and (h) VG staining images of new bone around the pillars implanted for 6 weeks, and quantification of BV/TV, Tb. N and Tb. Sp based on (g) as well as statistics of BIC ratios based on (h). Data are presented as mean ± SD, n = 4, $^{*}p < 0.05$, $^{**}p < 0.01$, $^{***}p < 0.001$, $^{****}p < 0.0001$, and NS: no significance.

with IL-4 (namely ST + IL-4) as controls, based on that MΦs evoked by LPS are M1 while stimulated by IL-4 are M2 [58]. The spread plate method (SPM)-tested photographs of bacterial colonies in Fig. 8a show that the STC_h-conditioned MΦs possess the ability to engulf *S. aureus* roughly similar to the ST + LPS-conditioned MΦs, and much higher than the MΦs conditioned by ST and ST + IL-4, owing to the distinct polarization phenotypes of MΦs derived by STC_h (mainly M1) and ST (mainly M2) within 24 h (Fig. 4a). This efficiency was further identified by TEM (Fig. 8b) and fluorescence staining (Fig. 8c) analyses of the arrays-conditioned MΦs that engulf *S. aureus*. Compared to the ST-conditioned MΦs, the STC_h-mediated MΦs uptake more *S. aureus* (white arrow marked in Fig. 8b) and internalize them adjacent to actin fibers of MΦs (Fig. 8c). These internalized bacteria have been demonstrated to firstly locate within phagosomes and keep alive, then to be transported to lysosomes for lysosomal degradation and eventually cleared [78].

We further implanted ST- and STC_h-arrayed pillars into *S. aureus*-infected femoral marrow cavities of S-D rats for 7 days to assess the phagocytosis of *S. aureus* by arrays-conditioned MΦs and their mediated MΦ polarization *in vivo*. The numbers of *S. aureus* adhered to the arrayed pillars and within peri-implant tissues were measured by rolling the pillars on blood agar plates and re-culturing for 24 h, and Giemsa staining of the tissue sections adjacent to PRS, respectively. At day 3 of implantation, the *S. aureus* adhered on the implanted pillars exhibit a decrease in number following ST + IL-4 > ST > STC_h > ST + LPS (Fig. 8d), inversely proportional to the bacteria phagocytosed by the pillars-conditioned MΦs *in vitro* (Fig. 8a), suggesting that STC_h array may trigger immune anti-bacteria with antibacterial rate as high as 99.8 % *in vivo* (right panel of Fig. 8d). Correspondingly, as shown in Fig. 8e, STC_h array makes the *S. aureus* within the peri-pillar tissue greatly reduce compare with ST array at each implantation time point of days 1, 3 and 7, even almost invisible at day 3 and thereafter. To validate the origin of immune anti-bacteria, we conducted the immunofluorescence staining of the tissue sections adjacent to PRS obtained at days 1, 3 and 7 of implantation, focusing on staining phenotypic markers CCR7 (specific for M1 MΦs) and Arg-1 (specific for M2 MΦs) together with cellular nuclei. Visibly, the MΦs within the tissue surrounding STC_h-arrayed pillar express CCR7 highly and Arg-1 lowly ($CCR7^{high}Arg\text{-}1^{low}$) on day 1, while express $CCR7^{low}Arg\text{-}1^{high}$ on day 7 (Fig. 8f). This may be attributed to the STC_h-released Co^{2+} induced M1 polarization of MΦs on day 1, resulting in engulfing *S. aureus* and consequently clearing *S. aureus* within peri-STC_h tissue later (Fig. 8e); the displayed M2 polarization of MΦs on day 7 is likely attributed to the role of STC_h nanoenzyme in scavenging ROS within local inflammatory environment, as supported by Fig. 4a–c. By contrast, the MΦs within the tissue surrounding ST-arrayed pillar express $CCR7^{high}Arg\text{-}1^{low}$ on day 7 (Fig. 8f). This may be attributed to the *S. aureus* infection (such as secreting LPS) induced M1 polarization of MΦs, leading to their phagocytosis of bacteria and consequently significant decrease of *S. aureus* within peri-ST tissue on day 7 (Fig. 8e).

The results depicted in Fig. 8a–f demonstrate that STC_h array can intensely trigger MΦs for immune anti-bacteria in *S. aureus*-infected femur of S-D rats at early stage and thereafter transit MΦs into pro-healing phenotype quickly. Owing to these effects, the STC_h-arrayed pillar was examined to show good osteogenic (Fig. 8g) and osseointegrative (Fig. 8h) abilities in *S. aureus*-infected femoral marrow cavities of S-D rats, which are slight low than those presented in uninfected case (Fig. 7a and b), but significantly higher than those presented by the ST-arrayed pillar in *S. aureus*-infected case (Fig. 8g and h).

4. Conclusion

A nanorod-like array of Co^{2+} and Co^{3+} co-doped sodium hydrogen titanate (STC_h) has been fabricated on Ti. STC_h array is shown to not only spontaneously release Co^{2+}, but also act as a novel nanoenzyme to scavenge ROS with this effect being enhanced over immersion. *In vitro*, STC_h nanoenzyme array derives BMSCs to differentiate into neurons and Schwann cells via releasing Co^{2+}, also elicits MΦs in a strong M1 response during a short period and thereafter in M2 response via Co^{2+} stimulus and later ROS scavenging, leading to the conditioned MΦs to considerably secrete neurogenic factors. Under the synergistic actions of the Co^{2+} and neurogenic factors, the nanoenzyme array promotes neuronal and Schwann cellular differentiation of BMSCs more significantly compared to sole Co^{2+} stimulus. This *in vitro* result is consistent with the rat endosseous neuronal differentiation of MSCs and formation of sensory and sympathetic nerves around STC_h. In rat bone, STC_h nanoenzyme reveals a strong role in accelerating neural network (especially sensory fibers) reconstruction, angiogenesis (particularly type-H capillaries) and subsequent osseointegration in normal case, and a strong antibacterial effect via phagocytosis of *S. aureus* by MΦs and osseointegration in infective case. Physiological neuronal functions such as calcium spark generation will be considered in our future research. In conclusion, this study provides a new insight into orchestrating endosseous neural network reconstruction for osseointegration without loading exogenous neurotrophins in implants.

Ethics approval and consent to participate

Male Sprague-Dawley (S-D) rats (~200 g weight) were employed for implantation of the pillars, which obeyed the guidelines and were approved by the Institutional Animal Care and Use Committee (IACUC) of Xi'an Jiaotong University (approval NO. XJTUAE2024-1921).

CRediT authorship contribution statement

Xinmei Cai: Writing – original draft, Visualization, Validation, Software, Methodology, Investigation, Formal analysis, Data curation. **Meng Yu:** Writing – original draft, Visualization, Software, Methodology, Investigation, Formal analysis, Data curation. **Bo Li:** Software, Methodology, Investigation. **Yingang Zhang:** Supervision, Methodology, Data curation. **Yong Han:** Writing – review & editing, Supervision, Resources.

Declaration of competing interest

Yong Han is an editorial board member for Bioactive Materials and was not involved in the editorial review or the decision to publish this article. All authors declare that there are no competing interests.

Acknowledgements

The authors greatly appreciate the financial support from the National Key Research and Development Program of China (Grant No. 2023YFC2412600) and National Natural Science Foundation of China (Grant No. 51971171).

Appendix A. Supplementary data

Supplementary data to this article can be found online at https://doi.org/10.1016/j.bioactmat.2024.08.005.

References

[1] D. Yu, B. Li, M. Yu, S. Guo, Z. Guo, Y. Han, Cubic multi-ions-doped Na_2TiO_3 nanorod-like coatings: structure-stable, highly efficient platform for ions-exchanged release to immunomodulatory promotion on vascularized bone apposition, Bioact. Mater. 18 (2022) 72–90, https://doi.org/10.1016/j.bioactmat.2022.01.039.

[2] R. Tao, B. Mi, Y. Hu, S. Lin, Y. Xiong, X. Lu, A.C. Panayi, G. Li, G. Liu, Hallmarks of peripheral nerve function in bone regeneration, Bone, Res. 11 (1) (2023), https://doi.org/10.1038/s41413-022-00240-x.

[3] Z. Li, C.A. Meyers, L. Chang, S. Lee, Z. Li, R. Tomlinson, A. Hoke, T.L. Clemens, A. W. James, Fracture repair requires TrkA signaling by skeletal sensory nerves, J. Clin. Invest. 129 (12) (2019) 5137–5150, https://doi.org/10.1172/jci128428.

[4] Q. Qin, S. Lee, N. Patel, K. Walden, M. Gomez-Salazar, B. Levi, A.W. James, Neurovascular coupling in bone regeneration, Exp. Mol. Med. 54 (11) (2022) 1844–1849, https://doi.org/10.1038/s12276-022-00899-6.

[5] C. Emanueli, P. Schratzberger, R. Kirchmair, P. Madeddu, Paracrine control of vascularization and neurogenesis by neurotrophins, Brit. J. Pharmacol. 140 (4) (2009) 614–619, https://doi.org/10.1038/10.1038/sj.bjp.0705458.

[6] Q.Q. Wan, W.P. Qin, Y.X. Ma, M.J. Shen, J. Li, Z.B. Zhang, J.H. Chen, F.R. Tay, L. N. Niu, K. Jiao, Crosstalk between bone and nerves within bone, Adv. Sci. 8 (7) (2021) 2003390, https://doi.org/10.1038/10.1002/advs.202003390.

[7] J.M. Brazill, A.T. Beeve, C.S. Craft, J.J. Ivanusic, E.L. Scheller, Nerves in bone: evolving concepts in pain and anabolism, J. Bone Miner. Res. 34 (8) (2019) 1393–1406, https://doi.org/10.1002/jbmr.3822.

[8] A. Andrzejewska, B. Lukomska, M. Janowski, Mesenchymal stem cells: from roots to boost, Stem Cell. 37 (7) (2019) 855–864, https://doi.org/10.1002/stem.3016.

[9] W. Jing, D. Zuo, Q. Cai, G. Chen, L. Wang, X. Yang, W. Zhong, Promoting neural transdifferentiation of BMSCs via applying synergetic multiple factors for nerve regeneration, Exp. Cell Res. 375 (2) (2019) 80–91, https://doi.org/10.1016/j.yexcr.2018.12.021.

[10] A.M. Sandoval-Castellanos, F. Claeyssens, J.W. Haycock, Biomimetic surface delivery of NGF and BDNF to enhance neurite outgrowth, Biotechnol. Bioeng. 117 (10) (2020) 3124–3135, https://doi.org/10.1002/bit.27466.

[11] H.N. Gregory, O. Guillemot-Legris, D. Crouch, G. Williams, J.B. Phillips, Electrospun aligned tacrolimus-loaded polycaprolactone biomaterials for peripheral nerve repair, Regen. Med. 19 (4) (2024) 171–187, https://doi.org/10.2217/rme-2023-0151.

[12] A. Zargar Kharazi, G. Dini, R. Naser, Fabrication and evaluation of a nerve guidance conduit capable of Ca^{2+} ion release to accelerate axon extension in peripheral nerve regeneration, J. Biomed. Mater. Res. A. 106 (8) (2018) 2181–2189, https://doi.org/10.1002/jbm.a.36425.

[13] Z. Yao, W. Yuan, J. Xu, W. Tong, J. Mi, P.C. Ho, D.H.K. Chow, Y. Li, H. Yao, X. Li, S. Xu, J. Guo, Q. Zhu, L. Bian, L. Qin, Magnesium-Encapsulated injectable hydrogel and 3D-engineered polycaprolactone conduit facilitate peripheral nerve regeneration, Adv. Sci. 9 (21) (2022), https://doi.org/10.1002/advs.202202102.

[14] M. Patel, H.J. Lee, S. Son, H. Kim, J. Kim, B. Jeong, Iron ion-releasing polypeptide thermogel for neuronal differentiation of mesenchymal stem cells, Biomacromolecules 21 (1) (2019) 143–151, https://doi.org/10.1021/acs.biomac.9b01096.

[15] Y.-X. Ma, K. Jiao, Q.-Q. Wan, J. Li, M.-Y. Liu, Z.-B. Zhang, W. Qin, K.-Y. Wang, Y.-z. Wang, F.R. Tay, L.-N. Niu, Silicified collagen scaffold induces semaphorin 3A secretion by sensory nerves to improve in-situ bone regeneration, Bioact. Mater. 9 (2022) 475–490, https://doi.org/10.1016/j.bioactmat.2021.07.016.

[16] S. Razavi, R. Seyedebrahimi, M. Jahromi, Biodelivery of nerve growth factor and gold nanoparticles encapsulated in chitosan nanoparticles for schwann-like cells differentiation of human adipose-derived stem cells, Biochem. Biophys. Res. Commun. 513 (3) (2019) 681–687, https://doi.org/10.1016/j.bbrc.2019.03.189.

[17] A.K. Podder, M.A. Mohamed, G. Tseropoulos, B. Nasiri, S.T. Andreadis, Engineering nanofiber scaffolds with biomimetic cues for differentiation of skin-derived neural crest-like stem cells to schwann cells, Int. J. Mol. Sci. 23 (18) (2022), https://doi.org/10.3390/ijms231810834.

[18] Y. Xuan, L. Li, X. Yin, D. He, S. Li, C. Zhang, Y. Yin, W. Xu, Z. Zhang, Bredigite-based bioactive nerve guidance conduit for pro-healing macrophage polarization and peripheral nerve regeneration, Adv. Healthcare Mater. 13 (8) (2023), https://doi.org/10.1002/adhm.202302994.

[19] G. Pandini, C. Satriano, A. Pietropaolo, F. Gianì, A. Travaglia, D. La Mendola, V. G. Nicoletti, E. Rizzarelli, The inorganic side of NGF: copper(II) and zinc(II) affect the NGF mimicking signaling of the N-terminus peptides encompassing the recognition domain of TrkA receptor, Front. Neurosci. 10 (2016), https://doi.org/10.3389/fnins.2016.00569.

[20] G.W. Ashley, J. Henise, R. Reid, D.V. Santi, Hydrogel drug delivery system with predictable and tunable drug release and degradation rates, Proc. Natl. Acad. Sci. USA 110 (6) (2013) 2318–2323, https://doi.org/10.1073/pnas.1215498110.

[21] I.S. Pires, P.T. Hammond, D.J. Irvine, Engineering strategies for immunomodulatory cytokine therapies: challenges and clinical progress, Advanced Therapeutics 4 (8) (2021), https://doi.org/10.3389/10.1002/adtp.202100035.

[22] J.L. Sun, K. Jiao, L.N. Niu, Y. Jiao, Q. Song, L.J. Shen, F.R. Tay, J.H. Chen, Intrafibrillar silicified collagen scaffold modulates monocyte to promote cell homing, angiogenesis and bone regeneration, Biomaterials 113 (2017) 203–216, https://doi.org/10.1016/j.biomaterials.2016.10.050.

[23] L. Bai, Z. Du, J. Du, W. Yao, J. Zhang, Z. Weng, S. Liu, Y. Zhao, Y. Liu, X. Zhang, X. Huang, X. Yao, R. Crawford, R. Hang, D. Huang, B. Tang, Y. Xiao, A multifaceted coating on titanium dictates osteoimmunomodulation and osteo/angio-genesis towards ameliorative osseointegration, Biomaterials 162 (2018) 154–169, https://doi.org/10.1016/j.biomaterials.2018.02.010.

[24] N. Yang, W. Cheng, H. Hu, M. Xue, X. Li, Y. Wang, Y. Xuan, X. Li, J. Yin, Y. Shi, S. Yan, Atorvastatin attenuates sympathetic hyperinnervation together with the augmentation of M2 macrophages in rats postmyocardial infarction, Cardiovasc. Ther. 34 (4) (2016) 234–244, https://doi.org/10.1111/1755-5922.12193.

[25] J. Wu, H. Xie, S. Yao, Y. Liang, Macrophage and nerve interaction in endometriosis, J. Neuroinflammation 14 (1) (2017), https://doi.org/10.1186/s12974-017-0828-3.

[26] I. Maldonado-Lasunción, N. O'Neill, O. Umland, J. Verhaagen, M. Oudega, Macrophage-derived inflammation induces a transcriptome makeover in mesenchymal stromal cells enhancing their potential for tissue repair, Int. J. Mol. Sci. 22 (2) (2021), https://doi.org/10.3390/ijms22020781.

[27] E. Vögelin, J.M. Baker, J. Gates, V. Dixit, M.A. Constantinescu, N.F. Jones, Effects of local continuous release of brain derived neurotrophic factor (BDNF) on peripheral nerve regeneration in a rat model, Exp. Neurol. 199 (2) (2006) 348–353, https://doi.org/10.1016/j.expneurol.2005.12.029.

[28] Y. Zhang, Y. Daaka, PGE_2 promotes angiogenesis through EP4 and PKA Cγ pathway, Blood 118 (19) (2011) 5355–5364, https://doi.org/10.1182/blood-2011-04-350587.

[29] P.M. Vidal, E. Lemmens, D. Dooley, S. Hendrix, The role of "anti-inflammatory" cytokines in axon regeneration, Cytokine, Growth Factors R. 24 (1) (2013) 1–12, https://doi.org/10.1016/j.cytogfr.2012.08.008.

[30] M. Noureddini, J. Verdi, S.A. Mortazavi-Tabatabaei, S. Sharif, A. Azimi, P. Keyhanvar, A. Shoae-Hassani, Human endometrial stem cell neurogenesis in response to NGF and bFGF, Cell Biol. Int. 36 (10) (2013) 961–966, https://doi.org/10.1042/cbi20110610.

[31] C.T. Wong, N. Ussyshkin, E. Ahmad, R. Rai-Bhogal, H. Li, D.A. Crawford, Prostaglandin E2 promotes neural proliferation and differentiation and regulates Wnt target gene expression, J. Neurosci. Res. 94 (8) (2016) 759–775, https://doi.org/10.1002/jnr.23759.

[32] J. Yuan, G. Huang, Z. Xiao, L. Lin, T. Han, Overexpression of β-NGF promotes differentiation of bone marrow mesenchymal stem cells into neurons through regulation of AKT and MAPK pathway, Mol. Cell. Biochem. 383 (1–2) (2013) 201–211, https://doi.org/10.1007/s11010-013-1768-6.

[33] R. Piovesana, A. Pisano, S. Loreti, R. Ricordy, C. Talora, A.M. Tata, Notch signal mediates the cross-interaction between M2 muscarinic acetylcholine receptor and neuregulin/ErbB pathway: effects on schwann cell proliferation, Biomolecules 12 (2) (2022), https://doi.org/10.3390/biom12020239.

[34] A. George, C. Kleinschnitz, M. Zelenka, J. Brinkhoff, G. Stoll, C. Sommer, Wallerian degeneration after crush or chronic constriction injury of rodent sciatic nerve is associated with a depletion of endoneurial interleukin-10 protein, Exp. Neurol. 188 (1) (2004) 187–191, https://doi.org/10.1016/j.expneurol.2004.02.011.

[35] E. Contreras, S. Bolívar, X. Navarro, E. Udina, New insights into peripheral nerve regeneration: the role of secretomes, Exp. Neurol. 354 (2022), https://doi.org/10.1016/j.expneurol.2022.114069.

[36] R. Leimeroth, C. Lobsiger, A. Lüssi, V. Taylor, U. Suter, L. Sommer, Membrane-bound Neuregulin1 type III actively promotes schwann cell differentiation of multipotent progenitor cells, Dev. Biol. 246 (2) (2002) 245–258, https://doi.org/10.1006/dbio.2002.0670.

[37] S. Lan, B. Jing, C. Yu, D. Yan, Z. Li, Z. Ao, M. Zhu, Protrudent iron single-atom accelerated interfacial piezoelectric polarization for self-powered water motion triggered fenton-Like reaction, Small 18 (2) (2021), https://doi.org/10.1002/smll.202105279.

[38] Y. Wan, J. Fang, Y. Wang, J. Sun, Y. Sun, X. Sun, M. Qi, W. Li, C. Li, Y. Zhou, L. Xu, B. Dong, L. Wang, Antibacterial zeolite imidazole frameworks with manganese doping for ommunomodulation to accelerate infected wound healing, Adv. Healthcare Mater. 10 (22) (2021), https://doi.org/10.1002/adhm.202101515.

[39] J. Li, J. Wen, B. Li, W. Li, W. Qiao, J. Shen, W. Jin, X. Jiang, K.W.K. Yeung, P. K. Chu, Valence state manipulation of cerium oxide nanoparticles on a titanium surface for modulating cell fate and bone formation, Adv. Sci. 5 (2) (2018) 1700678, https://doi.org/10.1002/advs.201700678.

[40] J. Zhou, L. Zhang, Y.-C. Huang, C.-L. Dong, H.-J. Lin, C.-T. Chen, L.H. Tjeng, Z. Hu, Voltage- and time-dependent valence state transition in cobalt oxide catalysts during the oxygen evolution reaction, Nat. Commun. 11 (1) (2020), https://doi.org/10.1038/s41467-020-15925-2.

[41] G. Liu, X. Wang, X. Zhou, L. Zhang, J. Mi, Z. Shan, B. Huang, Z. Chen, Z. Chen, Modulating the cobalt dose range to manipulate multisystem cooperation in bone environment: a strategy to resolve the controversies about cobalt use for orthopedic applications, Theranostics 10 (3) (2020) 1074–1089, https://doi.org/10.7150/thno.37931.

[42] Y.L.H.Y. Zhu, X.P. Gao, S.P. Ringer, Z.F. Zheng, D.Y. Song, J.C. Zhao, Phase transition between nanostructures of titanate and titanium dioxides via simple wet-chemical reactions, J. Am. Chem. Soc. 127 (18) (2005) 7, https://doi.org/10.1021/ja044689+.

[43] N. Li, L. Zhang, Y. Chen, M. Fang, J. Zhang, H. Wang, Highly efficient, irreversible and selective ion exchange property of layered titanate nanostructures, Adv. Funct. Mater. 22 (4) (2011) 835–841, https://doi.org/10.1002/adfm.201102272.

[44] S.-G.O.D.-H. Kim, C.-G. Cho, Effects of Cs and Na ions on the interfacial properties of dodecyl sulfate solutions, Colloid Polym. Sci. 279 (2001) 7, https://doi.org/10.1007/s003960000393.

[45] X. Han, G. He, Y. He, J. Zhang, X. Zheng, L. Li, C. Zhong, W. Hu, Y. Deng, T.Y. Ma, Engineering catalytic active sites on cobalt oxide surface for enhanced oxygen electrocatalysis, Adv. Energy Mater. 8 (10) (2017), https://doi.org/10.1002/aenm.201702222.

[46] X. Zhang, Y. Huang, B. Wang, X. Chang, H. Yang, J. Lan, S. Wang, H. Qiao, H. Lin, S. Han, Y. Guo, X. Zhang, A functionalized Sm/Sr doped TiO_2 nanotube array on titanium implant enables exceptional bone-implant integration and also self-antibacterial activity, Ceram. Int. 46 (10) (2020) 14796–14807, https://doi.org/10.1016/j.ceramint.2020.03.004.

[47] R.T.D.G.V. Gibbs, D.F. Cox, K.M. Rosso, N.L. Ross, A. Kirfel, T. Lippmann, W. Morgenroth, T.D. Crawford, Experimental bond critical point and local energy density properties determined for Mn-O, Fe-O, and Co-O bonded interactions for tephroite, Mn_2SiO_4, Fayalite, Fe_2SiO_4, and Co_2SiO_4 olivine and selected organic metal complexes: comparison with properties calculated for non-transition and transition metal M-O bonded interactions for silicates and oxides, J. Phys. Chem. A. 112 (2008), https://doi.org/10.1021/jp804280j.

[48] Z. Chen, J. Yuen, R. Crawford, J. Chang, C. Wu, Y. Xiao, The effect of osteoimmunomodulation on the osteogenic effects of cobalt incorporated beta-tricalcium phosphate, Biomaterials 61 (2015) 126–138, https://doi.org/10.1016/j.biomaterials.2015.04.044.

[49] H. Zhu, A. Yang, J. Du, D. Li, M. Liu, F. Ding, X. Gu, Y. Liu, Basic fibroblast growth factor is a key factor that induces bone marrow mesenchymal stem cells towards cells with Schwann cell phenotype, Neurosci. Lett. 559 (2014) 82–87, https://doi.org/10.1016/j.neulet.2013.11.044.
[50] J. Xue, J. Yang, D.M. O'Connor, C. Zhu, D. Huo, N.M. Boulis, Y. Xia, Differentiation of bone marrow stem cells into schwann cells for the promotion of neurite outgrowth on electrospun fibers, ACS Appl. Mater. Interfaces 9 (14) (2017) 12299–12310, https://doi.org/10.1021/acsami.7b00882.
[51] E.S. Jeon, J.H. Shin, S.J. Hwang, G.J. Moon, O.Y. Bang, H.H. Kim, Cobalt chloride induces neuronal differentiation of human mesenchymal stem cells through upregulation of microRNA-124a, Biochem. Biophys. Res. Commun. 444 (4) (2014) 581–587, https://doi.org/10.1016/j.bbrc.2014.01.114.
[52] G. Raspaglio, F. Filippetti, S. Prislei, R. Penci, I. De Maria, L. Cicchillitti, S. Mozzetti, G. Scambia, C. Ferlini, Hypoxia induces class III beta-tubulin gene expression by HIF-1α binding to its 3' flanking region, Gene 409 (1–2) (2008) 100–108, https://doi.org/10.1016/j.gene.2007.11.015.
[53] M. Maisel, H.-J. Habisch, L. Royer, A. Herr, J. Milosevic, A. Hermann, S. Liebau, R. Brenner, J. Schwarz, M. Schroeder, A. Storch, Genome-wide expression profiling and functional network analysis upon neuroectodermal conversion of human mesenchymal stem cells suggest HIF-1 and miR-124a as important regulators, Exp. Cell Res. 316 (17) (2010) 2760–2778, https://doi.org/10.1016/j.yexcr.2010.06.012.
[54] Y. Zhou, Y. Ni, K. Zhang, X. Liu, T. Yang, B. Wang, L. Fu, L. A, miR-21 promotes the differentiation of hair follicle-derived neural crest stem cells into Schwann cells, Neural Regen. Res. 9 (8) (2014), https://doi.org/10.4103/1673-5374.131599.
[55] B.E. Deverman, P.H. Patterson, Cytokines and CNS development, Neuron 64 (1) (2009) 61–78, https://doi.org/10.1016/j.neuron.2009.09.002.
[56] Gregg L. Semenza, Hypoxia-inducible factors in physiology and medicine, Cell 148 (3) (2012) 399–408, https://doi.org/10.1016/j.cell.2012.01.021.
[57] X. Yu, Q. Wan, X. Ye, Y. Cheng, J.L. Pathak, Z. Li, Cellular hypoxia promotes osteogenic differentiation of mesenchymal stem cells and bone defect healing via STAT3 signaling, Cell. Mol. Biol. Lett. 24 (1) (2019), https://doi.org/10.1186/s11658-019-0191-8.
[58] N. Wang, H. Liang, K. Zen, Molecular mechanisms that influence the macrophage M1-M2 Polarization Balance, Front. Immunol. 5 (2014), https://doi.org/10.3389/fimmu.2014.00614.
[59] S.-J. Park, K.-P. Lee, S. Kang, J. Lee, K. Sato, H.Y. Chung, F. Okajima, D.-S. Im, Sphingosine 1-phosphate induced anti-atherogenic and atheroprotective M2 macrophage polarization through IL-4, Cell. Signal. 26 (10) (2014) 2249–2258, https://doi.org/10.1016/j.cellsig.2014.07.009.
[60] S. Gordon, Alternative activation of macrophages, Nat. Rev. Immunol. 3 (1) (2003) 23–35, https://doi.org/10.1038/s41590-018-0117-z.
[61] W. Qiao, D. Pan, Y. Zheng, S. Wu, X. Liu, Z. Chen, M. Wan, S. Feng, K.M.C. Cheung, K.W.K. Yeung, X. Cao, Divalent metal cations stimulate skeleton interoception for new bone formation in mouse injury models, Nat. Commun. 13 (1) (2022), https://doi.org/10.1038/s41467-022-28203-0.
[62] J. Saha, D. Sarkar, A. Pramanik, K. Mahanti, A. Adhikary, S. Bhattacharyya, PGE_2-HIF1α reciprocal induction regulates migration, phenotypic alteration and immunosuppressive capacity of macrophages in tumor microenvironment, Life Sci. 253 (2020), https://doi.org/10.1016/j.lfs.2020.117731.
[63] A.B. Fernández-Martínez, J. Lucio-Cazaña, Intracellular EP2 prostanoid receptor promotes cancer-related phenotypes in PC3 cells, Cell. Mol. Life Sci. 72 (17) (2015) 3355–3373, https://doi.org/10.1007/s00018-015-1891-5.
[64] K. Nakamura, F. Tan, Z. Li, C.J. Thiele, NGF activation of TrkA induces vascular endothelial growth factor expression via induction of hypoxia-inducible factor-1α, Mol. Cell. Neurosci. 46 (2) (2011) 498–506, https://doi.org/10.1016/j.mcn.2010.12.002.
[65] S.-Y. Park, W. Ma, S.N. Yoon, M.J. Kang, J.-S. Han, Phospholipase D1 increases Bcl-2 expression during neuronaldifferentiation of rat neural stem cells, Mol. Neurobiol. 51 (3) (2014) 1089–1102, https://doi.org/10.1007/s12035-014-8773-y.
[66] J. Wang, X. Wang, Z. Sun, X. Wang, H. Yang, S. Shi, S. Wang, Stem cells from human-exfoliated deciduous teeth can differentiate into dopaminergic neuron-like cells, Stem Cell. Dev. 19 (9) (2010) 1375–1383, https://doi.org/10.1089/scd.2009.0258.
[67] G.-T. Yiang, Y.-L. Yu, K.-T. Lin, J.-N. Chen, W.-J. Chang, C.-W. Wei, Acetaminophen induces JNK/p38 signaling and activates the caspase-9-3-dependent cell death pathway in human mesenchymal stem cells, Int. J. Mol. Med. 36 (2) (2015) 485–492, https://doi.org/10.3892/ijmm.2015.2254.
[68] A.T. Regua, N.R. Aguayo, S.A. Jalboush, D.L. Doheny, S.G. Manore, D. Zhu, G. L. Wong, A. Arrigo, C.J. Wagner, Y. Yu, A. Thomas, M.D. Chan, J. Ruiz, G. Jin, R. Strowd, P. Sun, J. Lin, H.-W. Lo, TrkA interacts with and phosphorylates STAT3 to enhance gene transcription and promote breast cancer stem cells in triple-negative and HER2-enriched breast cancers, Cancers 13 (10) (2021), https://doi.org/10.3390/cancers13102340.
[69] A. Alizadeh, S.M. Dyck, H. Kataria, G.M. Shahriary, D.H. Nguyen, K.T. Santhosh, S. Karimi-Abdolrezaee, Neuregulin-1 positively modulates glial response and improves neurological recovery following traumatic spinal cord injury, Glia 65 (7) (2017) 1152–1175, https://doi.org/10.1002/glia.23150.
[70] Z. Xu, A.P. Kusumbe, H. Cai, Q. Wan, J. Chen, Type H blood vessels in coupling angiogenesis-osteogenesis and its application in bone tissue engineering, J. Biomed. Mater. Res. B-Appl. Biomater. 111 (7) (2023) 1434–1446, https://doi.org/10.1002/jbm.b.35243.
[71] L. Saxen, Effect of tetracycline on osteogenesis in vitro, J. Exp. Zool. 162 (3) (1966) 25, https://doi.org/10.1002/jez.1401620305.
[72] H. Puchtler, S.N. Meloan, M.S. Terry, On the history and mechanism of alizarin and alizarin red S stains for calcium, J. Histochem. Cytochem. 17 (2) (2016) 110–124, https://doi.org/10.1177/17.2.110.
[73] R.Y. Huang, L.M. Miller, C.S. Carlson, M.R. Chance, In situ chemistry of osteoporosis revealed by synchrotron infrared microspectroscopy, Bone 33 (4) (2003) 514–521, https://doi.org/10.1016/s8756-3282(03)00233-3.
[74] C. Zhan, M. Huang, J. Chen, Y. Lu, X. Yang, J. Hou, Sensory nerves, but not sympathetic nerves, promote reparative dentine formation after dentine injury via CGRP-mediated angiogenesis: an in vivo study, Int. Endod. J. 57 (1) (2023) 37–49, https://doi.org/10.1111/iej.13989.
[75] W. Liu, J. Li, M. Cheng, Q. Wang, Y. Qian, K.W.K. Yeung, P.K. Chu, X. Zhang, A surface-engineered polyetheretherketone biomaterial implant with direct and immunoregulatory antibacterial activity against methicillin-resistant Staphylococcus aureus, Biomaterials 208 (2019) 8–20, https://doi.org/10.1016/j.biomaterials.2019.04.008.
[76] M. Soleimani Hosseinzadeh, N. Hatami, Z.-H. Wei, Antibacterial properties of nanoporous graphene oxide/cobalt metal organic framework, Biomater. Adv. 104 (2019), https://doi.org/10.1016/j.msec.2019.109862.
[77] B. Erdem, A. Dayangaç, İ.K. Şahin, The presence of mmetals and antibiotics resistant bacteria in arable manure soils, Acta Phys. Pol., A 132 (3) (2017) 570–571, https://doi.org/10.12693/aphyspola.132.570.
[78] C.-O. Wong, S. Gregory, H. Hu, Y. Chao, V.E. Sepúlveda, Y. He, D. Li-Kroeger, W. E. Goldman, H.J. Bellen, K. Venkatachalam, Lysosomal degradation is required for sustained phagocytosis of bacteria by macrophages, Cell Host Microbe 21 (6) (2017) 719–730.e6, https://doi.org/10.1016/j.chom.2017.05.002.